博士論文

Optogenetic study of neural activity and connectivity in deep brain structures of non-human primates

（非ヒト霊長類の脳深部構造における
神経活動および神経結合の光遺伝学的研究）

田　村　啓　太

CONTENTS *page*

ABSTRACT

The optogenetic approach to studying the primate brain has unparalleled potential for uncovering circuit-based mechanisms of cognitive functions. Here, I describe a series of works on the application of optogenetics to primate deep brain structures. For photostimulation and electrophysiological recording, I developed a glass-coated tungsten optrode that has a rigid, smooth, thin structure and can be inserted deep into the brain. For precise targeting of virus injection into deep brain structures, I developed a stick-shaped ultrasmall syringe-pump system mounted on a hydraulic manipulator that uses the same coordinate system as electrophysiological mapping of the target area. I also developed a metal-backboned glass injectrode that enables electrophysiological recording and pressure-injection at the same locus, enabling the target area to be identified using neural activity. I applied these optogenetics methods to *in vivo* models. The injection system resulted in a successful expression of channelrhodopsin-2-enhanced-yellow-fluorescent-protein even in the perirhinal cortex, the deepest part in the macaque brain. *In vivo*, fiber-optic fluorescence measurements made with the optrode clearly detected channelrhodopsin-2-enhanced-yellow-fluorescent-protein expression. In the rat, functional magnetic resonance imaging during photostimulation of the thalamic posterior medial nucleus revealed a focal activation in the secondary somatosensory

area corresponding to the histologically identified thalamic projection. In the monkey thalamus, light-responsive single units were isolated and categorized according to spike discharge probability. These methodologies have had substantial impact on the field and have already been put to use. They enable neural circuits of cognition to be studied, even at the bottom of the macaque inferior temporal cortex.

Abbreviations

ANOVA, analysis of variance

AP, anterior-posterior

ChR2-EYFP, channelrhodopsin-2- enhanced-yellow-fluorescent-protein

Deg, degree

Em_{535}, emission in 535-nm band

Ex, excitation

EYFP, enhanced yellow fluorescent protein

fMRI, functional magnetic resonance imaging

GFAP, glial fibrillary acidic protein

IA, interaural line

LM, lateral-medial

MRI, magnetic resonance imaging

PSTH, peri-stimulus time histogram

Rf_{469}, reflection in 469-nm band

ROI, region-of-interest

TE, echo time

TR, repetition time

INTRODUCTION

The optogenetic approach to the primate brain is a breakthrough research model that has huge potential to advance our understanding of the neural mechanisms of cognitive functions. In the field of memory research, optogenetics has primarily been applied to study the rodent brain during simple conditioning paradigms [1-3]. Study of the monkey brain will contribute to this field by allowing researchers to elucidate circuit-based mechanisms underlying the formation and retrieval of explicit memories for episodes or objects. In the rhinal cortex of macaque monkeys, which is located in the bottom of the brain, bridging the hippocampus and the ventral visual stream, learned visual objects are coded by a population of neurons [4-6]. Optogenetic dissection of the macaque rhinal cortex will reveal how mnemonic information is processed and used for adaptive behaviors of monkeys.

However, the macaque brain is structurally complex and several times larger than the rodent brain, and only a limited number of animals are trained for cognitively demanding tasks; therefore, significant technical advancements are required before optogenetics can be used to study the deep regions of macaque monkey brain during cognitive tasks. In macaque monkeys, opsin genes for

light-gated ion channels or ion pumps [7] are introduced by localized injection of viral vectors into the target of interest [8, 9]. The target region must be accurately localized in each animal, without miss-localization or injection fault. Light for photostimulation is delivered by optical fibers inserted into the brain with or without a combined recording-electrode [10]. The optical probe used for the photostimulation must correctly target the virus-injected region to ensure effective photostimulation. All of these procedures (virus injection, photostimulation and physiological recording) should be minimally invasive to allow reproducible results to be obtained over long experimental periods from individual animals.

Addressing these issues requires the development of a new methodological infrastructure that has been optimized for deep brain structures in the primate. First, a minimally invasive combined optical and electrical probe (optrode) is required to allow simultaneous photostimulation and electrophysiological recording. Second, an adaptable coordinate management system for virus injection is required to allow accurate injection of the virus into a target region-of-interest that has been electrophysiologically mapped. Third, a minimally invasive combined injection needle and electrode (injectrode) is required to allow the position of the injection needle to be guided by electrophysiological monitoring of neural activity.

Successful application of optogenetics *in vivo* requires successful expression of the transgenes, and tools that can accurately measure the effect of photostimulation at a global as well as a local level. In long-term experiments with chronic preparations, the expression of the transgenes introduced by the virus injection should be confirmed before photostimulation experiments are conducted in task-playing animals. This can be done by measuring the fluorescence of the marker proteins via optical fibers within the optrode [11, 12]. The impact of photostimulation on remote brain regions is of a major interest in living animals. Functional magnetic resonance imaging (fMRI) measures hemodynamic responses across the whole-brain, and can be used to visualize whole-brain activity [13]. For the electrophysiological analysis of optogenetically activated neurons, the quality of extracellular recordings made with the optrode should be sufficient to allow isolation of single units. The spike discharge probability of single units in response to high-frequency repetitive light pulses [14] is another point to be discussed in optogenetics-assisted electrophysiology to putatively categorize the recorded units into directly or indirectly photoactivated cells.

In this thesis, I describe the details of these methodological developments and present results from the application of these methods to rats and monkeys.

MATERIALS AND METHODS

All experiments except for the preparation of viral vectors were conducted by the author.

All animal procedures complied with the National Institutes of Health (NIH) Guide for the Care and Use of Laboratory Animals and were approved by the Institutional Review Committee of the University of Tokyo School of Medicine. All surgical procedures were performed under aseptic and analgesic condition, and all efforts were made to minimize the suffering and number of animals used.

Anatomical brain areas were identified according to a rat brain atlas [15] and a macaque brain atlas [16].

Fabrication of the glass-coated tungsten optrode

In the first process, optical fibers and tungsten wires were sharpened. To obtain sharpened optical fibers that efficiently conduct light to the tip, the graded index silica fibers (cladding, 125 μm; numerical aperture, 0.275; GIF625, Thorlabs) were selected and pulled by a micropipette puller. The pulled fiber had a conical tip with a 5 mm taper. The tungsten wires (diameter, 50 μm; #715550, A-M Systems) were electrochemically etched. In the second process, four optical fibers were thinly

coated with an appropriate amount of silicon lubricant (see below) and assembled together with the tungsten wire in polyimide tubes (i.d., 300 μm; o.d., 350 μm; #120, MicroLumen) and a glass capillary (i.d., 400 μm; o.d., 500 μm, PYREX) so that these fibers symmetrically surrounded the centered tungsten wire (Fig. 1A, right). The assembly was fixed at the base with cyanoacrylate adhesive. In the third process, by pulling the capillary, the optical fibers and the tungsten wire were integrally coated with a thin layer of glass (Fig. 1B). Finally, the glass coating at the tungsten tip was removed so that the optrode had the impedance suited for electrophysiological recording.

In the glass-coating process, the amount of lubricant was critical. Excess lubrication prevented the glass coating from adhering to the tungsten, while insufficient lubrication caused cracking of the optical fibers due to adhesion. The specifications of the optrode were adjusted as follows: exposed tip length, 30–70 μm; impedance, 0.2–1.2 MΩ (1 kHz); inter-tip distance (tungsten wire to optical fibers), 300–700 μm; and total length, 4-5 cm (for rats) or 10-12 cm (for monkeys). The basal part of the optrode was reinforced with a semi-hard type heat shrink tube. The optrode could be held and manipulated by a conventional manipulator.

Inspection of the illumination property

The light emission property was examined by a stereoscopic fluorescence microscope (VB-G05, Keyence) and ImageJ software (NIH). For the lateral view, the optrode was observed in fluorescein solution. For axial views, the optrode was positioned so that its tip lightly touched a fluorescent screen made of two small fragments of cover glass sandwiching a drop of fluorescein solution (Fig. 3C). The light spot on the screen was observed from the opposite side in five different illumination conditions: four single-fiber conditions in which the light is conducted to only one of the fibers 1, 2, 3 or 4; and an all-fibers condition in which the light was conducted to all of four fibers (Fig. 3D). Emission from a single optical fiber was observed in the air.

The spatial illumination pattern was analyzed in the axial images. In every single-fiber condition, a triangular dark quadrant was inevitably generated due to shading by the tungsten tip. In order to analyze the spatial distribution of the intensity, a cross-shaped region-of-interest (cross-ROI) consisting of two long rectangular ROIs (2×0.2 mm^2) crossing at right angles was defined. The cross-point of the cross-ROI located on the center of the spot and one of the four arms of the cross-ROI divided the dark quadrant in half. Small ROIs (0.2×0.2 mm^2 square) were

defined on every arm of the cross-ROI at the point 0.5 mm from the cross-point (named 0-, 90-, 180-, and 270-deg ROI; the ROI on the dark quadrant was defined as 0-deg ROI). In the all-fibers condition, four small ROIs were defined in the positions corresponding to 0-deg ROIs, which were defined in every single-fiber condition. A cross-ROI was also defined in the same position as that of the single-fiber condition with fiber 1. Intensity was normalized to the maximum for each image to evaluate the relative distribution within each light spot. The numerical aperture was calculated from the angle of the light cone measured in the lateral view image. For the statistical analysis, the following tests (significance criteria) were used: paired *t*-test ($P < 0.05$), and one-way ANOVA ($P < 0.05$) followed by *t*-test with a Bonferroni correction ($P < 0.05/6$).

Fabrication of the stick-shaped syringe-pump system

A stick-shaped syringe-pump was customized for the purpose of virus injection into the brain from a commercially available model (SAP series, Takasago Electric Inc) by changing the column size to 10 μL and the minimum step of the plunger to 2 nL. Different column sizes were also available for different volumes of the injected viruses. The power and the step pulses for the built-in stepping motor

were supplied by USB ports of a controller PC. The stick-shaped syringe-pump was directly connected to the replaceable injection needle or injectrode and was held by a hydraulic manipulator (MO-95C, Narishige) when inserting the injectrode or injection needle into the brain.

Fabrication of the metal-backboned glass injectrode

A pipette design that coupled a glass pipette and a stainless steel needle [17] was modified to make an injectrode that was suitable for the deep structures of the monkey brain. First, a glass capillary (length, 15 cm; i.d., 400 μm; o.d., 500 μm; PYREX) was pulled by a pipette puller to make a thin, closed tip with a taper longer than 10 mm (Fig. 5D top). Second, a parylene-coated ultrathin tungsten wire (length, >20 cm; diameter, 12.5μm [approx. 1.2 MΩ at 1 kHz] or 20 μm [aprox. 0.5 MΩ at 1 kHz]; California Fine Wire Company) and a blunt-end stainless steel injection needle (length, 11 cm; replaceable needle type; 30 G; ILS) was inserted into the pipette as far as the diameters allowed (Fig. 5D middle). Visible-light-curable adhesive (LocTite 4304, Henkel) was actively permeated from the back end of the pipette by providing negative pressure with a normal micro syringe connected to the stainless steel needle. The motion of the adhesive was carefully observed and

permeation was stopped just prior to the tip of the stainless steel needle. Third, after curing the adhesive by illuminating with a halogen lamp, the tips of the pipette and the wire were ground together using a pipette grinder (EG-3, Narishige) at an angle of 30 deg to form a sharp tip with the desirable diameter (aprox. 70 μm for the perirhinal cortex of monkeys; Fig. 5D, bottom). The free end of the tungsten wire was stripped of insulation and connected to the amplifier.

Viral vector preparation

Adeno-associated virus vector, AAV5-CaMKIIa-ChR2(H134R)- EYFP was purchased from University of North Carolina Vector Core.

Lentiviral vectors were kindly produced by Dr. Y. Ohashi (The University of Tokyo) [18, 19]. For the generation of the transfer vector pCL20c-MSCV-hChR2-EYFP-WPRE (Lenti-MSCV-ChR2-EYFP-WPRE), *Spe*I/*Xba*I-digested hChR2-EYFP fragment from pcDNA3.1-hChR2-EYFP (kindly provided by Dr. K. Deisseroth) was inserted into *Eco*RI/*Not*I-digested pCL20c MSCV-GFP (kindly provided by Dr. Arthur W. Nienhuis) [20] by blunt-end ligation to replace the GFP coding sequence. The *Cla*I-digested WPRE fragment from CS-CA-MCS (kindly provided by Dr. H. Miyoshi) [21] was subcloned into the *Cla*I site of the above

constructed plasmid, pCL20c-MSCV-hChR2-EYFP. For the generation of the transfer vector pCL20c-CMV-hChR2-EYFP-WPRE (Lenti-CMV-ChR2-EYFP-WPRE), *Eco*RI/*Age*I-digested CMV promoter from CS-CDF-CG-PRE (kindly provided by Dr. H. Miyoshi) was inserted into *Mlu*I/*Eco*RI-digested pCL20c-MSCV-hChR2-EYFP-WPRE by blunt-end ligation to replace the MSCV promoter. With cultured HEK293T cells, two lentiviral vectors were prepared as described previously [18, 19]. For the titration of viral stocks, cultured HEK293T cells were transduced, transfection efficiency was estimated by counting the EYFP-positive cells using an EPICS XL flow cytometer with EXPO32 software (Beckman Coulter), and the functional titer was calculated from a linear range.

Anesthesia procedures

Monkeys: during general anesthesia in all operations, SpO2, heart rate, and blood pressure were continuously monitored and body temperature was maintained by a heat pad and a blanket. In surgical operations for implanting recording chambers, general anesthesia was induced by a mixture of medetomidin (0.03 mg. $kgBW^{-1}$, i.m.) and midazolam (0.3 mg. $kgBW^{-1}$, i.m.), and maintained by pentobarbital (4 mg. $kgBW^{-1}$ h^{-1}, i.v.) and xylazine (0.2 mg. $kgBW^{-1}$, i.m.)

supplemented as needed. Adequate anesthesia was confirmed by the lack of withdrawal responses to skin pinching. Before scalp incision and suturing, local anesthesia (lidocaine, 1 mg. mL^{-1}) was added. During surgical operation, antibiotic (cefazolin, 10 mg. $kgBW^{-1}$ h^{-1}, i.v.) was administered. During the postsurgical recovery period, monkeys were received analgesics (ketoprofen, 1.5 mg. $kgBW^{-1}$ day^{-1}, i.m.) and antibiotics (ampicillin, 20 mg. $kgBW^{-1}$ day^{-1}, i.m.), and their behavior and food intake were observed carefully in their home cages for a week. For the MRI acquisition, virus injection, electrophysiological recording, photostimulation and fluorescence measurements, general anesthesia was induced by a mixture of medetomidin (0.03 mg. $kgBW^{-1}$, i.m.) and midazolam (0.3 mg. $kgBW^{-1}$, i.p.) and maintained by continuous administration of propofol (6 mg. $kgBW^{-1}$ h^{-1}, i.v.) and xylazine (0.4 mg. $kgBW^{-1}$ h^{-1}, i.m.) supplemented as needed [22].

Rats: rats were anesthetized by pentobarbital (40 mg. $kgBW^{-1}$, i.p.), or a mixture of ketamine (90 mg. $kgBW^{-1}$ i.p.) and xylazine (10 mg. $kgBW^{-1}$, i.p.) in surgical operation for virus injection and fluorescence measurements, and by urethane (1.2 g. $kgBW^{-1}$, i.p.) in fMRI acquisition. Adequate anesthesia was confirmed by the lack of withdrawal responses to hindlimb pinching. During all

procedures, body temperature was maintained by a heat pad. After the surgery, antibiotic ointment (gentamicin, 0.1%) was applied to the scalp incision.

Viral vector injection

For the virus injection in the primate thalamus (mediodorsal, ventroanterior and ventrolateral nuclei) and the inferior temporal cortex (perirhinal cortex), four male macaque monkeys (*Macaca mulatta*, 7.5 kg, monkey 1; *Macaca fuscata*, 7.8 kg, monkey 2; *Macaca mulatta*, 9.5 kg, monkey 3; *Macaca fuscata*, 7.6 kg, monkey 4) were anesthetized and implanted with a MRI-compatible chamber (LM, +15.5 mm, and AP, +9.5 mm from interaural line (IA) for thalamus; LM, 0.0 mm, and AP, +11.0 mm from IA for perirhinal cortex in monkey 3; LM, -14.0 mm, and AP, +17.5 mm from IA for perirhinal cortex in monkey 4). After the recovery over a week, the depth of the target area was checked by conventional microelectrode recordings. Then, the viral vectors were injected using the recording chamber under anesthesia. The functions of the viral vector stocks had been checked in the rat thalamus before the injection into the monkeys.

MRI images of the monkey brain were obtained prior to the injection using a 4.7-T MRI scanner (Bruker) [23] with a three-dimensional modified driven

equilibrium Fourier transform (MDEFT; TR/TE = 2560/15 ms, matrix = 256×256×240, voxel = 500×500×500 μm^3). To estimate the coordinates in the chamber on MRI images, a plastic grid (1.5-mm spacing square grid) filled with Isodine® ointment (Meiji) was attached to the chamber during the scan.

For the monkey thalamus (monkey 1 and 2), the viral suspension (Lenti-CMV-ChR2-EYFP-WPRE, titer 1.3×10^{10} TU. mL^{-1}) was injected at a depth of approximately 18 (monkey 1) or 24 mm (monkey 2) (pre-determined by MRI and electrophysiological profiles; 2 μL. $site^{-1}$; 1 (monkey 2) or 2 (monkey 1) sites. $track^{-1}$ separated by 1 mm; 8 tracks in a 1.5 mm grid; 200 nL. min^{-1}) by the stick-shaped syringe-pump connected to a beveled 30 gauge stainless steel needle.

For the monkey perirhinal cortex (monkey 3 and monkey 4), the viral suspension (AAV5-CaMKIIa-ChR2(H134R)-EYFP-WPRE, titer 4×10^{12} GC. mL^{-1}) was injected using the stick-shaped syringe-pump connected to the metal-backboned injectrode. The manipulator holding the syringe-pump system was attached to a recording chamber with a tilt angle of 10 deg from medial to lateral in monkey 3 and a tilt angle of 7.5 deg from posterior to anterior in monkey 4. The injectrode was slowly inserted into the brain while unit activity was monitored on the oscilloscopes. The bottom cortex was identified by the transition of neural activity from white

matter to gray matter at a depth of approximately 40 mm from the dorsal surface of the brain. Then, the tip was positioned so that it was located below the border of white matter and gray matter and kept shallower than the bottom surface of the brain by carefully monitoring neural activity to ensure that there was no spillover outside of the cortex. Injection was made after a 10 min rest (2 μL. site^{-1}, 1 site. track^{-1} separated by 3 mm, 200 nL. min^{-1} in monkey 3; 1.5 μL. site^{-1}, 2 site. track^{-1} separated by 1.5 mm, 200 nL. min^{-1} in monkey 4).

For the injection into the rat thalamus, Wistar rats (10–20 wks old, 170–360 g) were anesthetized and small craniotomy was made. Using a metal-backboned glass micropipette without a tungsten wire, the viral suspension (Lenti-MSCV-ChR2-EYFP-WPRE for the fiber-optic fluorescence detection and the functional MRI, titer 1.6×10^{9} TU. mL^{-1}; or Lenti-CMV-ChR2-EYFP-WPRE for a function-check, titer 1.3×10^{10} TU. mL^{-1}) was injected into ventral posterolateral nucleus (LM -2.5 mm, and AP, -3.0 mm from bregma; -5 mm from dura; 2 μL. site^{-1}, 1 site, 100 nL. min^{-1}) or posterior medial nucleus (LM, -2.25 mm, and AP -3.75 mm from bregma; -5 mm from dura; 2 μL. site^{-1}, 1 site, 100 nL. min^{-1}).

Fiber-optic fluorescence detection

EYFP expression was examined *in vivo* by fluorescence measurements via the optical fiber [11, 24]. For the excitation of EYFP, three of four optical fibers of the optrode were connected to the 473-nm laser system described previously [19] and a train of light pulses was applied (200-ms pulse duration, 0.2–0.5 Hz; 110–220 μW at input, kept constant during the sessions). For the detection of fluorescence emission, the optical path of the remaining fiber was split and connected to either of two high-sensitive photodetectors (PDF10A, Thorlabs) installed with a bandpass filter (535/22 nm or 469/35 nm, Thorlabs). The 535-nm photodetector measured EYFP emission (Em_{535}), while the 469-nm photodetector measured the reflection and fluctuation of excitation light (Rf_{469}). Photodetector output signal (voltage) was stored in a PC (Recorder, Plexon) and analyzed by MATLAB (Mathworks).

The performance of the fiber-optic fluorescence detection system was examined in the rat thalamus. A rat that had been injected with the viral vector (Lenti-MSCV-ChR2-EYFP-WPRE) was anesthetized (pentobarbital, 40 mg. $kgBW^{-1}$), and the optrode was inserted into two sites: the first track for the expressing site (“on-track”; LM -2.5 mm, and AP -3.0 mm from bregma) and the second track for the non-expressing site (“off-track”; LM, -0.5 mm, and AP, -3.0 mm from bregma). Intensity profiles of Em_{535} and Rf_{469} were obtained in 200-μm steps,

and the values were normalized to each baseline (the mean across the depth from 0.5 mm to 2.0 mm). Electrolytic lesion marks were created (negative current, 20 μA; 120 s. site^{-1}) at the following depth: 1 mm and 3 mm for “on-track”; 1 mm and 5 mm for “off-track”. The rat was left to recover for an additional 5 days. In the subsequent histological analysis, the recording tracks and the depths were reconstructed by observing the lesion marks in the nuclear-stained sections. The intensity profile along the “on-track” was obtained from the EYFP image (ImageJ). To compare the Em_{535} profile obtained *in vivo* and the EYFP fluorescence profile obtained by histology, the baseline (the mean across the depth from 0.5 mm to 2.0 mm)-subtracted value was normalized to the maximum for each profile.

fMRI during photostimulation

Images were obtained using a 4.7-T MRI scanner (BioSpec 47/40,Bruker BioSpin) with an actively shielded gradient coil (100 mT. m^{-1}), and a quadrature surface RF coil for rats (Bruker). For anatomical images, a fast-spin-echo sequence (TR/TE = 3000/24 ms, matrix = 256×256×17, voxel = 200×200×650 μm^3) was used. For functional images, a gradient echo echo-planer-imaging sequence (EPI; TR/TE= 3000/23.5 ms, flip angle = 80 deg, 1shot, matrix = 95×60×15, voxel = 600×600×650

μm^3) was used.

The rat was anesthetized and then fixed on an MRI compatible cradle (SRP-AR, Narishige) that was customized so that the surface RF coil with an open window was mounted just on the head of the rat (Fig. 7A). The eyes of the rat were covered by surgical tape to ensure that there was no visual input from the photostimulation. The glass-coated optrode (45-mm long) was inserted into the POm through a small craniotomy by the MRI-compatible micromanipulator [23], while the neural responses to the photostimulation were electrophysiologically monitored on oscilloscopes (473-nm laser, 1 mW at input, 50-ms pulses at 0.2 Hz). The tip of the optrode was positioned at 500 μm deeper than the depth which the light-evoked neural responses were maximal, where 500 μm is the approximate distance between the tungsten tip and the tip of the optical fibers. After setting the optrodes in the stimulation position, the exposed skull was covered with agar gel (2%) to reduce susceptibility artifacts in EPI.

Functional imaging during photostimulation was performed using a standard block design (Fig. 7B) [22, 25]. Each run of functional imaging was consisted of 12 simulation-ON blocks (7 EPI volumes [21 s] per block) interleaved with stimulation-OFF blocks (14 EPI volumes [42 s] per block). The four initial

volumes of each run were discarded to obtain a steady-state EPI signal. Photostimulation was delivered during stimulation-ON blocks using the following parameters: 473-nm light (4 mW in four fibers, at input), and 15-ms pulses at 20 Hz [13]. In total, six runs of functional imaging were conducted.

Whole-brain activation maps were calculated as described previously [22, 25] using the statistical parametric mapping toolbox (SPM5; http://www.fil.ion.ucl.ac.uk/spm) on MATLAB. Functional images were realigned and then smoothed with a Gaussian kernel (1.0-mm full-width at half-maximum). Activation maps (*t*-score maps) were computed using voxel-wise statistics based on the general linear model implemented in SPM5. The significance level of activation was set at $P < 0.05$ and corrected for multiple comparisons using the false discovery rate (FDR) [26].

Fluorescence measurements, photostimulation and recording of single-unit activity

For the electrophysiological recording of neural activity, the neural signal was amplified (2×10^4), filtered (low cut, 50~500 Hz; high cut, 10 kHz) and stored in a PC (20~50 kHz, Recorder). Unit activities were isolated offline with the Offline Sorter software (Plexon) by feature-based (e.g., principal components) waveform

analysis [27, 28]. A given unit was considered as a single-unit when the number of spikes within the interspike interval of 2 ms did not exceed 1% of the total in the autocorrelogram, which is an indicative of the refractory period [27-30]. Response properties of isolated units were analyzed by NeuroExplorer (Nex Technologies) and MATLAB (Mathworks).

For fiber-optic measurements of the depth distribution of ChR2-EYFP fluorescence in the monkey perirhinal cortex, the optrode was gradually inserted into the vector injected region, and the fluorescence intensity was measured in 500 μm (30-38 mm from the dorsal surface) or 250 μm steps (38-43.5 mm from the dorsal surface). The depth of the measurements was confirmed by the depth of the bottom of the brain (please note that the perirhinal cortex locates at the bottom of the brain) that was identified according to the change in the electrophysiological signal. The fluorescence intensity was normalized to the baseline (mean across the depth from 30 to 35 mm).

For the electrophysiological recording and photostimulation in the monkey thalamus, the optrode was inserted into the vector-injected region of thalamus. While repetitively applying photostimulation of 473-nm light pulses (10-, 200- or 500-ms pulse duration, 0.5 or 1 Hz; maintained at ~ 3.9 mW from input), single-unit

activities that changed firing rate during the photostimulation periods were searched for along tracks down to the bottom of the thalamus by audio and waveform monitoring.

For the comparison between the depths distribution of light-responsive units and EYFP fluorescence in the monkey thalamus, the approximate minimum light power for unit excitation was measured online by audio monitoring of its activity for each light-responsive unit encountered on the track. The response for an additional 60 photostimulation pulses was then recorded with a light power approximately twofold to the threshold of each unit (as a population, 30-750 μW from input). The fluorescence profile along the same track was obtained in 250 μm steps with the fiber-optic measurements, and the value was normalized to the baseline (mean across the depth from 21.5 mm to 24.5 mm).

For the precise control of the action potential generation, and for the categorization of recorded units into light-activated and synaptically-activated cells, trains of short light pulses (5-ms duration per pulse; 1, 5, 10, 20 and 40 Hz per unit; 10 pulses per train in 15-second interval; 10 trains per frequency) were delivered [1, 14, 31, 32]. Then, the dependency of the spike latency and spike reliability on the frequency of light pulses was examined. Spike response reliability at each frequency

of light pulses was calculated as the probability that at least one action potential is generated during a time window in the 2nd to 10th light pulse delivery of each train. 50 ms (at 1, 5, 10, and 20 Hz) or 25 ms (at 40 Hz) from the light pulse onset was used for the time window.

Histological analysis

Monkeys and rats were deeply anesthetized by pentobarbital and then perfusion fixed with and 4% paraformaldehyde and subjected to histological analysis as described previously [18, 19].

For immunofluorescence staining of macaque thalamus, 28-μm thick sections were incubated for 12 hours at 4 °C with three primary antibodies; rabbit anti-GFP (1:2000, MBL), mouse anti-NeuN (1:1000, Millipore), and chicken anti-GFAP (1:500, Millipore). Then the sections were incubated for 1 hour at 37 °C with three secondary antibodies: AlexaFluor488-conjugated goat anti-rabbit-IgG (1:1000, Invitrogen), AlexaFluor546-conjugated goat anti-mouse-IgG (1:1000, Invitrogen), and AlexaFluor647-conjugated goat anti-chicken-IgG(Y) (1:1000, Invitrogen).

For the histological analysis of EYFP expression in the rats, coronal brain

sections of 40-μm thickness were observed. To visualize the gliosis by electrolytic lesion marks or the cortical laminar structures, some sections were stained for nuclei (Hoechst 33258, 1 mg. mL^{-1}; MolecularProbes).

Fluorescence images were obtained using a fluorescence microscopy (BZ-9000, Keyence) or a confocal laser scanning microscopy (TCS-SPE, Leica).

RESULTS

Optimization of optogenetic approach

Glass-coated tungsten optrode

Background concepts: To optically manipulate and electrophysiologically record neuronal activity *in vivo*, optrodes, combined optical/electrical probes, have been utilized [10, 27, 29, 33, 34]. Among previous studies conducted with rodents, the majority of optrodes have been fabricated by directly gluing a bare optical fiber to the outside of an independent electrode. While this is a simple design for coupling the two materials, there are some concerns about its invasiveness in recording: roughness of the surface and the tip, toxicity of a chemical glue, and fragility of the materials coupling. Another factor to be considered is the size of the monkey brain: perirhinal cortex, for example, is located 45 millimeters from the dorsal surface of the brain. Given these issues on the invasiveness and the brain size, optogenetic investigation in the deep areas of primate brain in chronic experiments [35] requires an optrode incorporating the following characteristics. First, the tip should be sharp and smooth to reduce friction that causes tissue damages. Second, the shank should be sufficiently long, straight, and stiff for correct insertion into deep targets. Third, the illuminated area by the optrode should be wide for manipulating substantial

population of neurons [11, 32].

The glass-coated tungsten microelectrode [36, 37] has been widely used in single-unit recordings in chronically prepared animals. This popularity is partly because the metal tip is more robust and enables stable recording with a high signal-to-noise ratio compared to other electrodes, such as glass micropipette electrodes, and also because the glass has more suitable characteristics as a coating material with regard to its impedance, durability, and surface smoothness compared to resins such as epoxy and parylene [38]. In a method for fabricating a glass-coated tungsten microelectrode, a glass capillary into which a sharpened tungsten wire is inserted is pulled by a pipette puller to collapse the glass onto the tungsten wire for insulation. This method is potentially general enough to enclose other materials in addition to the tungsten wire.

Realization: I fabricated an optrode by glass-coating a tungsten wire and optical fibers. Figure 1A shows the design of the glass-coated tungsten optrode. A single optrode consisted of four sharpened graded-index optical fibers, one sharpened tungsten wire, and the glass coating. To illuminate the region around the tip from multiple directions, optical fibers surrounded the tungsten wire symmetrically (Fig. 1A, right). The assembly of materials was integrally coated with

a thin layer of glass by pulling a glass capillary over it. The silicon lubrication was essential to avoid cracking of the optical fiber (for details of the fabrication, see Materials and Methods).

Figure 1B shows a finished glass-coated optrode. The tips of the sharpened optical fibers were tightly bound to the tungsten wire by the inward collapsing force of the coating glass. Except for the tungsten tip, the optrode was totally covered with the thin glass layer. This resulted in the smooth transition of the surface structure from the tungsten tip to the optrode shank without a substantial gap, compared to a conventional design in which the blunt-end optical fiber is directly glued to the electrode (Fig. 2A). The glass-coated tip was durable enough for repeated penetrations of the rat brain through intact dura matter (Fig. 2B) and remained intact after multiple uses in monkeys.

I examined how the glass-coated optrode illuminated the region around the tip. A bare sharpened optical fiber emitted light from the conical part of the tip (approximately 50 μm) but not from the tapered side wall (Fig. 3A), suggesting that the photoconduction property of the graded index optical fiber was maintained after the sharpening process. From the glass-coated tip of a typical optrode, light was emitted in a conical pattern (Fig. 3B), which had a half angle of 45 degrees and

numerical aperture of 0.71. This value was substantially larger than that of a cleaved non-sharpened fiber (numerical aperture of 0.275; data from the spec. sheet).

The light cone was further observed from the axial direction (Fig. 3C) in five different illumination conditions: four single-fiber conditions and one all-fibers condition (Fig. 3D). In every single-fiber condition in which one of four optical fibers was recruited, a dark triangular area ("quadrant") was inevitably generated due to shading by the tungsten wire (four images at the corners in Fig. 3D; the asymmetric distribution in Fig. 3E, left). The intensity of the dark quadrant (defined as 0-deg ROI) was significantly smaller than those of the other three bright quadrants (90-, 180-, and 270-deg ROIs in Fig. 3F, left; $P < 3\times10^{-5}$ by one-way ANOVA and $P < 5\times10^{-3}$ by *t*-test). In the all-fibers condition, however, dark quadrants that had been observed in single-fiber conditions disappeared (the center image in Fig. 3D; the symmetric distribution in Fig. 3E, right), as confirmed by the significant increase of the 0-deg ROI intensity (3F, right; $P < 3\times10^{-4}$ by paired *t*-test). Thus, with illumination from multiple directions, the glass-coated optrode illuminated the region around the tip without generating a dark quadrant otherwise shaded by the optrode itself.

Stick-shaped syringe-pump and metal-backboned injectrode

Background concepts: To massively express transgenes in the target region, viral vectors are injected through an injection needle by pressure exerted by a microsyringe. It is critically important to inject viruses and insert optrodes into the same location. An implantable cannula-system is the standard for reproducible viral injection and optrode targeting in rodents [39]; however, there is no established method for reproducible viral injection and optrode targeting in deep brain structures of macaques. To share the same coordinate system, the microelectrode, injection needle, syringe-pump and an optrode should be handled by the same hydraulic manipulator that is used to electrophysiologically map the target region. To control injection pressure and speed, the needle should be connected directly to a microsyringe that is mounted on a syringe-pump without any tubing [40] to reduce dead volume.

The shank of the injection needle should be long and rigid so that it can be inserted deep into the brain. The tip should be thin and smooth like a glass pipette to minimize tissue damage and reduce the backflow of the injected solution [41]. It is highly desirable for the injection needle to be used to monitor neuronal activity at the injection site so that this information can be used to finely adjust the position of

the tip. For this purpose, some studies have reported the use of injection-electrodes, or injectrodes, made of an electrode and a stainless steel or glass pipette injection needle [8, 42-44], and other studies have reported injectrodes made of a multi-barrel glass capillary [45-49] or a metal-plated glass pipette [50]. However, the structural invasiveness, the complexity of the fabrication procedure, and the complexity of the overall setup of these designs are not optimal.

Realization: I used a stick-shaped ultrasmall syringe-pump with built-in mechanics that had been originally developed for a different purpose and attached a glass column and a plunger that had been customized for virus injection to the stick-shaped stepping motor drive (Fig. 4A). The minimum injection step was 2 nL for a 10-uL design. The length, diameter and weight of the full syringe-pump system (column plus motor drive) were 12 cm, 8.8 mm and 30 g respectively. This syringe-pump was small and light enough to be mounted on the hydraulic manipulator conventionally used for recordings in chronically prepared monkeys (Figs. 4B and 4C). By directly connecting this syringe-pump to the injection needle, injection pressure was provided with minimal dead volume to increase the control accuracy. By using different adapters for the syringe-pump, microelectrodes and optrodes, it was possible to hold and insert each piece of equipment into the target in

the coordinate system that was defined by the manipulator and the recording chamber.

I developed a glass pipette-based injectrode for performing virus injection and unit recording at the same location in the brain (Fig. 5A). A glass pipette was backboned by a stainless steel injection needle (Figs. 5B, top, and 5C, left) and used to enclose a parylene-insulated ultrathin tungsten wire (Figs. 5B, bottom, and 5C). At the tip, the tungsten edge shared the same tilted plane as the edge of the pipette (Fig. 5C), allowing extracellular recording within the diameter of the tip of the pipette (approx. 70 μm; Figs. 5A, insets, and 5C, right). The lateral surface of the injectrode was seamless along the 12-cm-long shaft and rigid enough to be inserted to deep brain locations. In fabrication (Fig. 5D), the stainless steel needle and a parylene-coated tungsten wire inserted into the glass pipette and sealed with light-curable adhesive. Then, the tip was ground to obtain a co-ground surface of the tungsten and the pipette (for details, see Materials and Methods).

Optogenetic study of *in vivo* models

Fiber-optic detection of gene expression

To detect the expression of the transgenes that was introduced by the virus

injection *in vivo*, I constructed a fiber-optic fluorescence measurement system and examined the performance of the glass-coated optrode in the readout of the fluorescence emitted by the marker protein EYFP *in vivo* (Fig. 6). Figure 6A shows the diagram of the readout system. The 473-nm excitation light illuminated the region around the tip. The 535-nm fluorescence emission (Em_{535}) and the 469-nm background reflection (Rf_{469}) were collected from the optical fiber tip, and measured separately by the photodetectors installed with bandpass filters.

The optrode was inserted into the rat thalamus injected with a lentiviral vector carrying the ChR2-EYFP transgene (Fig. 6B). On the track near the injection site ("on-track"), the Em_{535} profile showed a prominent peak around the depth of 4–6 mm (yellow trace in Fig. 6C). At the "off-track" site located 2 mm from "on-track", in contrast, the Em_{535} profile did not show a substantial peak (orange trace in Fig. 6C, inset). Em_{535} profiles were macroscopically independent of the Rf_{469} profile (blue traces in Fig. 6C). Thus, the Em_{535} peak was location-specific and did not correspond to the increase in the 469-nm band, indicating that the Em_{535} peak represented the wavelength-elongated fluorescence signal.

To confirm that the observed fluorescence signal was emitted by EYFP, the Em_{535} profile was compared with the actual EYFP expression pattern via histological

analysis (Figs. 6D and 6E). In the coronal histological section (Fig. 6D), the recording tracks (yellow and orange arrows) and the depths (vertical scale bar) were reconstructed by identifying the electrolytic lesion marks (arrow heads). The "on-track" EYFP fluorescence profile scanned from the histological section consistently overlapped with the "on-track" Em_{535} profile recorded *in vivo* (Fig. 6E). These results indicate that the glass-coated optrode can be used for detection of the EYFP expression *in vivo*.

fMRI of the photoactivated thalamocortical system

During fiber-optic observation of ChR2-EYFP fluorescence in the rat thalamus, neurons at the stimulation site responded to the photostimulation. To examine whether the local activation of the thalamus with the glass-coated optrode propagated to more remote regions, I conducted fMRI during photostimulation (Fig. 7). The glass-coated optrode was inserted into the posterior medial nucleus of thalamus (POm) of an anesthetized rat in which ChR2-EYFP was expressed. fMRI was then performed using an EPI sequence to visualize the whole-brain hemodynamic response to the photostimulation (Figs. 7A and 7B). When repetitive 473-nm light pulses were applied to the POm, a significant increase in the blood

oxygenation-level-dependent (BOLD) signal (t = 7.88, P < 0.001, corrected for multiple comparisons) was observed in the lateral part of the cortical region ipsi-lateral to the stimulated site ("+4-mm" slice in Fig. 7C, and Fig. 7D). This cortical activation site was located 4 mm anterior to the optrode track and was not affected by susceptibility artifacts or heating [51] caused by the optrode. At the local stimulation site in the POm, a relatively weak BOLD signal response (t = 4.18, P < 0.05, corrected for multiple comparisons) was observed ("0-mm" slice in Fig. 7C). The low strength of this response may be due to a lower cell density [52], a smaller number of intra-area excitatory connections [53], and a lower intra-area interaction [54] in the thalamus than in the cortex, which could all result in less oxygen consumption in the thalamus than in the cortex. The longer distance between the thalamus and the receiver RF coil and susceptibility artifacts caused by the optrode may also have reduced the MRI signal in the thalamus.

Subsequent histological analysis of the same rat revealed focal expression of ChR2-EYFP at the injection site (POm; "0-mm" slice in Fig. 7E). In the ipsilateral cortical region, axon terminals that originated in the POm were clustered mainly in the granular layer of the secondary somatosensory area (SII; Fig. 7F), which is the primary target of POm [55]. This cluster of POm axon terminals was

located 4 mm anterior to the histologically identified optrode track, in a location that was consistent with the fMRI results (compare “0-mm” and “+4-mm” slices in Figs. 7C and 7E). These results indicate that the focal BOLD signal in the cortex reflected the activity in the area SII that received the axonal projection from the optogenetically-activated POm neurons. Thus, the local neural activity evoked by the glass-coated optrode propagated toward a more remote brain region in accordance with the anatomical connectivity.

Gene transfer in deep region of macaque brain

By the stick-shaped syringe-pump and the metal-backboned injectrode, I performed the injection of a viral vector (AAV5-CaMKIIa-ChR2(H134R)-EYFP) into the perirhinal cortex of the macaque brain, a deep region 45 mm below the dorsal surface of the brain (Fig. 8A, left). The hydraulic manipulator (Figs. 4B and 4C) was used to finely adjust the depth of injectrode based on neural activity. The tip of the injectrode was positioned in the middle depth of the gray matter by carefully identifying the point at which the activity transitioned from the white matter characterized by the lack of unit activity to the gray matter characterized by frequent unit activities. Six weeks after injection, the expression of ChR2-EFYP was focally

confined to the perirhinal cortex of a macaque monkey (Figs. 8A, right, and 8B). This demonstrates that the injection system can be used to inject a viral vector into targets located deep within the brain, with neural activity used to guide the injectrode position.

The expression of ChR2-EYFP in the perirhinal cortex was measured *in vivo* by the fiber-optic fluorescence detection system in another monkey. The glass-coated optrode was inserted into the target while repeatedly measuring the fluorescence of EYFP (Fig. 8C, left). The Em_{535} profile showed a prominent peak around the depth of perirhinal cortex, about 43 mm from the dorsal surface of the brain (yellow trace in Fig. 8C, right). Em_{535} profiles were macroscopically independent of the Rf_{469} profile (white trace in Fig. 8C, right). Thus, the expression of transgenes in the deep region of the macaque brain can be checked by the fiber-optic fluorescence detection system.

Recording of the photoactivated single units

Finally, I conducted the fluorescence detection, the photostimulation and the extracellular recording of single-unit activities in the monkey thalamus. Monkeys were injected with a lentiviral vector carrying the ChR2-EYFP transgene

into the thalamic region (Fig. 9A). Immunohistochemical analysis revealed the expression of ChR2-EYFP in neurons that were positive for a neuronal marker NeuN and negative for a glial marker GFAP (Fig. 9B). The glass-coated optrode was slowly inserted while repetitive photostimulation pulses were applied via its optical fibers. Light-responsive single-units that changed firing rates during photostimulation were searched for along tracks down to the bottom of the thalamus. Light-responsive single-units were successfully isolated from the monkey thalamus (Figs. 9C to 9F). In unit separation, spike waveforms of the isolated unit recorded during light-off and light-on periods were similar to each other (Fig. 9C), and were separated from waveforms of other units (Fig. 9D). Autocorrelograms in both periods revealed the existence of the refractory period (Fig. 9E). These results demonstrated that the increase in the number of spikes during light-on period (Fig. 9F) reflected the increase in the level of spike generation by the isolated unit but not the infiltration of other multiunit spikes.

The light-responsive single-units recorded in the monkey thalamus generated spikes in response to repetitive short light-pulses (Fig. 10). Their response properties were consistent with those in previous studies in rodents [1, 14, 31], reporting that spike reliability at higher frequencies of light pulses is higher in

ChR2-expressing neurons that are directly activated by light, but lower in neurons that are indirectly activated by synaptic input from other ChR2-expressing neurons. In the monkey thalamus, putative ChR2-expressing units (units 1 and 2 in Fig. 10) reliably generated spikes even at higher frequencies of light pulses (Figs. 10B, and 10C, top), and their response latency and the jitter of latency were smaller (Figs. 10A, and 10C, bottom). By contrast, putative synaptically-activated units (units 3 and 4 in Fig. 10) generated spikes only at lower frequencies of light pulses (Figs. 10B, and 10D, top), and their response latency and the jitter of latency were relatively larger (Figs. 10A, and 10C, bottom). These results demonstrate that by using the present optrode, individual action potentials of ChR2-expresing neurons can be triggered using short light pulses in a time-locked manner.

Next the depth distribution of light-responsive units and EYFP fluorescence were compared (Fig. 11). In a track near viral injection sites (dotted line in Fig. 11A, left), 10 light-responsive single-units were encountered in total (PSTHs of all units in Fig. 11B). Also, a substantial increase in Em_{535} intensity was detected on the same track (yellow trace in Fig. 11A, right). The peak in Em_{535} profile and the depth distribution of the light-responsive single-units consistently overlapped with each other (Fig. 11A, right). Thus, by using the glass-coated optrode, the

ChR2-EYFP-expressing region was macroscopically localized in the monkey brain *in vivo*, and neuronal activity was successfully manipulated and recorded in that region. These results demonstrate that the present optrode enables optogenetic investigation even in deep areas of the primate brain.

DISCUSSION

I have developed methodological infrastructure for chronic optogenetic experiments in macaque monkeys, which includes a glass-coated tungsten optrode, a stick-shaped syringe-pump system and a metal-backboned glass injectrode. I have shown that these devices can be used for *in vivo* optogenetic experiments, as they can be used to effectively inject viral vectors into deep targets, detect fluorescence fiber-optically, and photostimulate and record neural activities at single-cell and whole-brain.

Compared with a conventional optrode, in which a thick optical fiber is glued to an electrode, the glass-coated optrode described in this work is likely to have less friction with the brain tissue, thus reducing the risk of mechanical damage and optical deterioration due to tissue or a blood clot. In addition, the biocompatibility is likely to be better because no chemical glue used to bind the materials is exposed. The structural and optical specifications of the glass-coated optrode can be optimized for different purposes by changing the materials and the fabrication protocols. Thus, the glass-coated optrode is a minimally-invasive and adaptable tool that is well suited for repeated uses in monkeys trained to perform cognitively demanding tasks.

The stick-shaped syringe-pump and the metal-backboned injectrode successfully injected the ChR2-EYFP-carrying viral vector into the perirhinal cortex of the macaque monkey. The stick-shaped syringe-pump weighs 30 g and is more than ten times lighter than other syringe pumps that have been popular in rodent experiments [18, 19, 39, 40, 56], which weigh a few to several hundred grams. The metal-backboned injectrode allowed unit recordings and pressure-injection at exactly the same site, which is usually possible only with an iontophoretic micropipette electrode. The external structure of the present injectrode is indistinguishable from a glass pipette, which can be taken to reflect the simplest and least invasive injection needle [41]. These properties will enable site-selective pressure-injections into brain regions including cortical columns/layers and subcortical nuclei that can be identified by neural activity *in vivo*. Thus, the combination of the stick-shaped syringe-pump and the metal-backboned injectrode held by a hydraulic manipulator provide an optimal injection setup for chronically-prepared macaque monkeys.

The site of ChR2-EYFP expression was macroscopically identified *in vivo* using fiber-optic fluorescence measurements. Fluorescence measurements were made using two independent optical fibers within a single glass-coated optrode: one

for excitation light delivery and one for fluorescence emission readout. This separate excitation/readout design with the glass-coated optrode could allow the detectors to measure small changes in the light collected from the tip of the readout fiber without being affected by substantial internal reflection of the excitation light within the fiber-optic system. The present system will be beneficial not only in checking the expression of the transgenes, but also in experiments in which a fluorescently-labeled region is targeted *in vivo* (e.g., a retro- or antero-gradely labeled population of neurons or axons). Fiber-optic measurements of population calcium signals [57, 58] with reporters like OGB-1 or GCaMPs in the deep regions of behaving monkeys during fMRI is one interesting application of this method.

In the fMRI study, BOLD signal activation was present in the cortex not only in the local activation site in the thalamus. The present result is promising, as it indicates that optogenetic activation of the local circuits by using the glass-coated optrode effectively propagated toward downstream neural circuits, which is a prerequisite for behavioral impacts. This effective activation is partly supported by the wide illumination property of the glass-coated optrode which can activate a larger population of neurons within the thalamus.

The activity of light-responsive single-units in the thalamus of the monkey

was successfully recorded during photostimulation. The performance of the glass-coated optrode in isolating and holding single-unit activities was comparable to that of conventional glass-coated tungsten microelectrodes that have been widely used in chronic recordings from the macaque brain [59], possibly owing to the sharp and smooth structure. These properties will enable single-unit studies combined with optogenetics in the deep regions of the macaque brain, which, to date, have been held back by the invasive nature of the available optrodes. The neuronal responses to photoactivation or photoinhibition may be different in different brain regions depending on the intrinsic cell properties. For example, thalamic relay neurons that express voltage-gated calcium ion channels (Ca_vs) can paradoxically result in an increase in low-threshold spikes [60] by lowering the membrane potential by ArchT- or NpHR-mediated photoinhibition. Thus, the effects of photostimulation must be electrophysiologically analyzed before performing behavioral tests in all target brain areas including deep regions.

Taken together, the methodologies developed and described in this thesis are well optimized for the brain of macaque monkeys. A part of these works has been published [12] and has had a substantial impact on other researchers inside and outside of the primate neuroscience community: the glass-coated optrode system has

been recognized as a promising approach for optogenetic stimulation and for measuring gene expression in deep brain structures [61-63] and has already been put into use to investigate neural circuits. The methodological developments mean that, the perirhinal cortex, the deepest part in the macaque brain, is now within the scope of optogenetic dissection. Optogenetic manipulation of this area and the areas to which it is connected will reveal the mechanisms of explicit-memory processing based on the causality between circuit and function. I am currently working on research in this area.

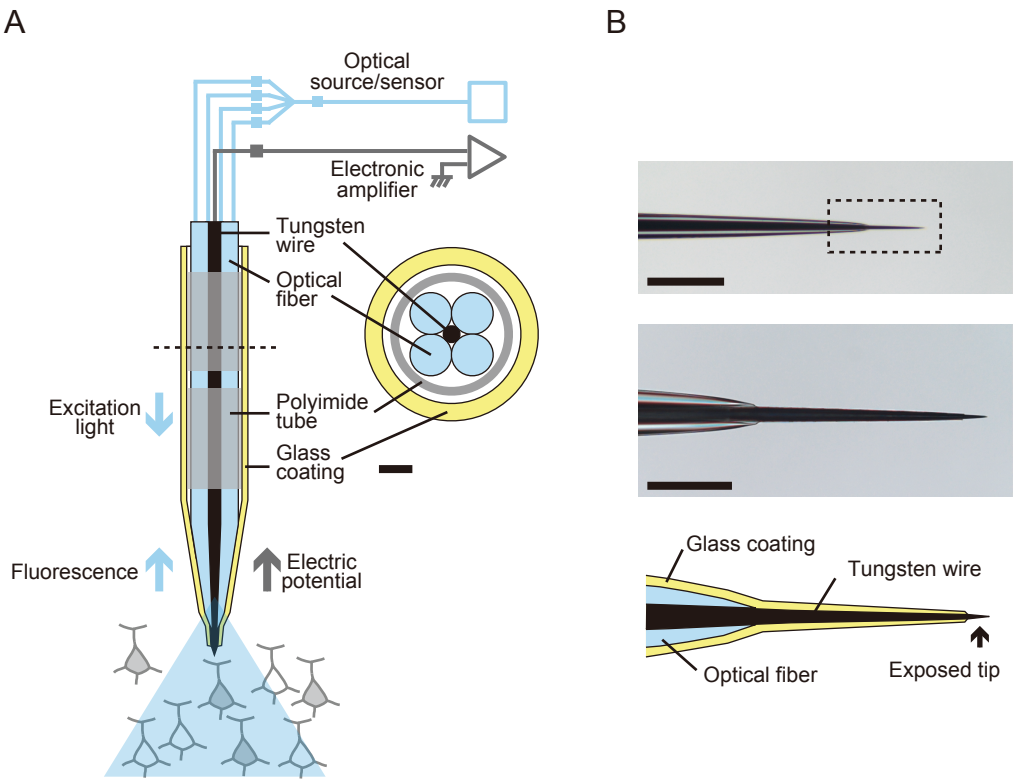
A
Optical source/sensor
Electronic amplifier
Tungsten wire
Optical fiber
Excitation light
Polyimide tube
Glass coating
Fluorescence
Electric potential
B
Glass coating
Tungsten wire
Optical fiber
Exposed tip

Figure 1

Figure 1. The glass-coated tungsten optrode. (**A**) A schematic drawing of a global structure from lateral (left, not drawn to scale) and axial (right) views. Sharpened optical fibers surround the sharpened tungsten wire to illuminate the tip region from multiple directions. Scale bar, 100 μm; dotted line, the level of axial view. (**B**) Tip structure from lateral views. Lower (top) and higher (middle, dotted area on top panel) magnification images, and a schematic drawing (bottom). Optical fibers are tightly bound to the tungsten shank without a substantial gap. These materials are integrally coated with a thin glass layer that simultaneously insulates the tungsten wire except for the tip (~50 μm). Note that the transparent parts on the left end are the sharpened optical fibers but not the glass-coating. Scale bars, 1000 μm (top), 200 μm (middle).

A

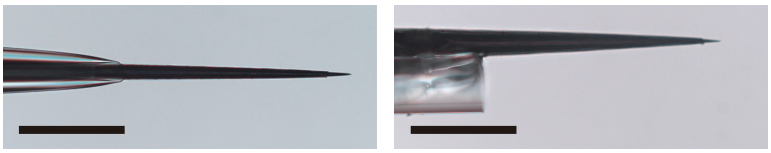

B

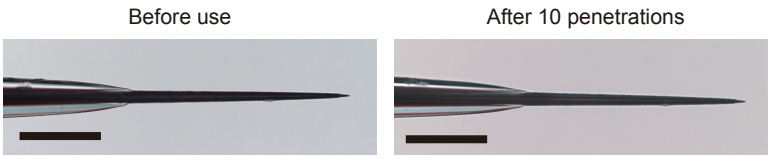

Figure 2

Figure 2. Structural advantages of the glass-coated optrode. (**A**) Left, the tip of the glass-coated optrode (the same optrode that appears in the Fig. 1B). Right, the tip of an optrode made by directly gluing a blunt-end optical fiber to the outside of a conventional glass-coated tungsten microelectrode with chemical adhesive. Please note that diameter of this blunt-end fiber (125 μm) is still thinner than those of popular fibers (>200 μm) that appear in other studies. Scale bar, 250 μm. (**B**) The tip of a glass-coated optrode before (left) and after (right) repeated penetrations into the brain of a rat through the dura matter. Enclosure of the optical fibers and a tungsten wire remained intact, showing the robustness of the tip structure.

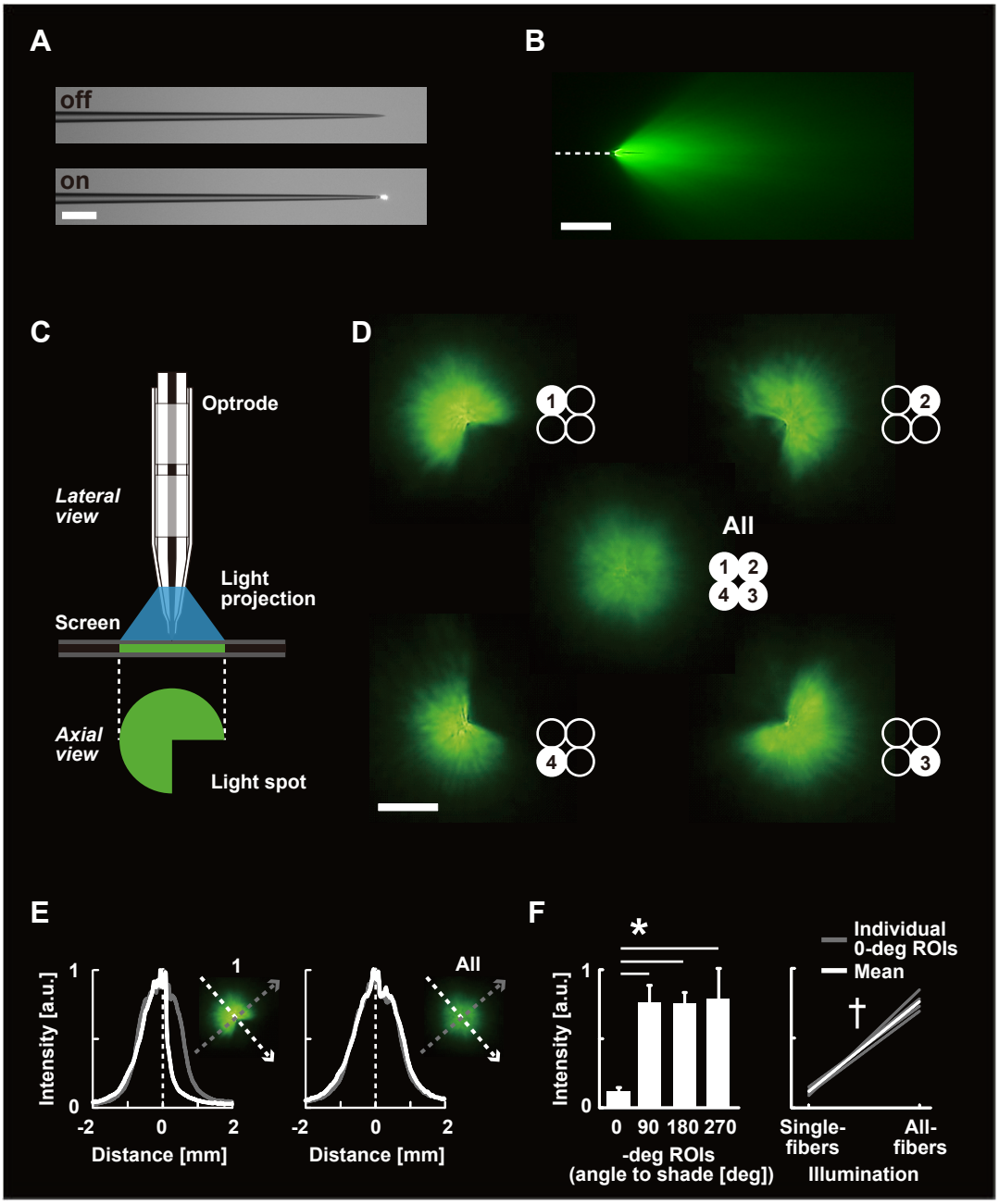
A
off
on
B
C
Optrode
Lateral view
Light projection
Screen
Axial view
Light spot
D
1
2
All
1 2
4 3
4
3
E
Intensity [a.u.]
1
0
1
All
-2 0 2
Distance [mm]
-2 0 2
Distance [mm]
F
*
Intensity [a.u.]
1
0
0 90 180 270
-deg ROIs
(angle to shade [deg])
Individual 0-deg ROIs
Mean
†
Single-fibers
All-fibers
Illumination

Figure 3

Figure 3. Optical advantages of the glass-coated optrode. (**A**) The tip of a single sharpened optical fiber in light-off (top) and light-on (bottom) states. Scale bar, 200 μm. (**B**) The light cone generated by a glass-coated optrode in the fluorescein solution from the lateral view. All four optical fibers were recruited. Dotted line, optrode position; scale bar, 1 mm. (**C to F**) Analyses of the spatial distribution of the intensity. (C) A photographing scheme for the axial views of the light cone. Light was projected vertically onto the fluorescent screen. (D) Light spots generated in five different illumination conditions: four single-fiber conditions and an all-fibers condition (insets illustrate the conditions: the numbers represent recruited fibers). Note that the pictures are not rotated for display purposes. The intensity in the all-fibers condition was lower because the aperture time was shorter. Scale bar, 1 mm. (E) Spatial intensity profiles in single-fiber (left, "1") and all-fibers (right, "all") conditions along the cross-shaped ROIs represented as gray and white arrows in insets. Intensity values were normalized to the maximum for each image. (F) ROI analyses. Left, the intensities of four ROIs (0, 90, 180 and 270 deg) across four single-fiber conditions. The 0-deg ROI corresponds to a triangular dark quadrant. Right, a comparison of the intensities of four 0-deg ROIs between single-fiber and all-fibers conditions. Intensity values were normalized to the maximum for each image. Error bars, standard deviation. *, $P < 3\times10^{-5}$ (one-way ANOVA) and $P < 5\times10^{-3}$ (*t*-test); †, $P < 3\times10^{-4}$ (paired *t*-test).

A

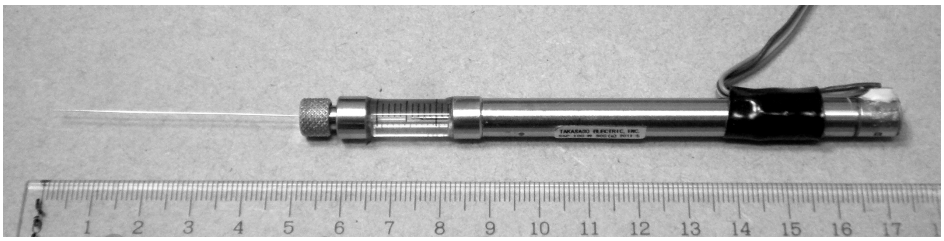


Injection needle, Injectrode
Column
Motor drive
Control cable

B

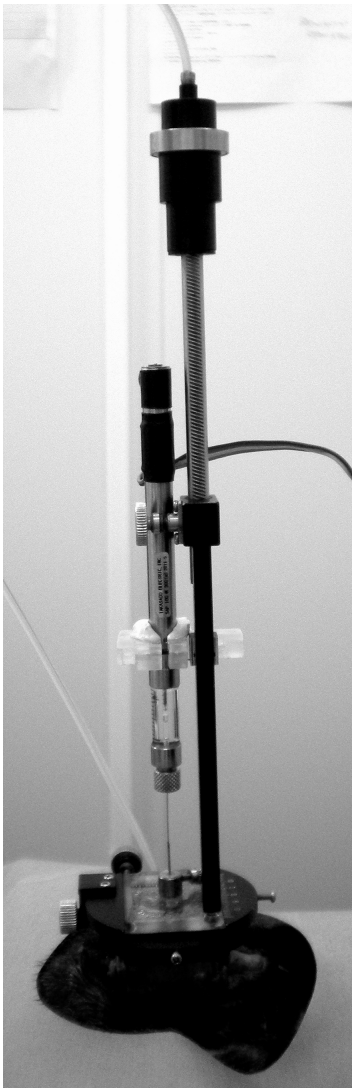

C

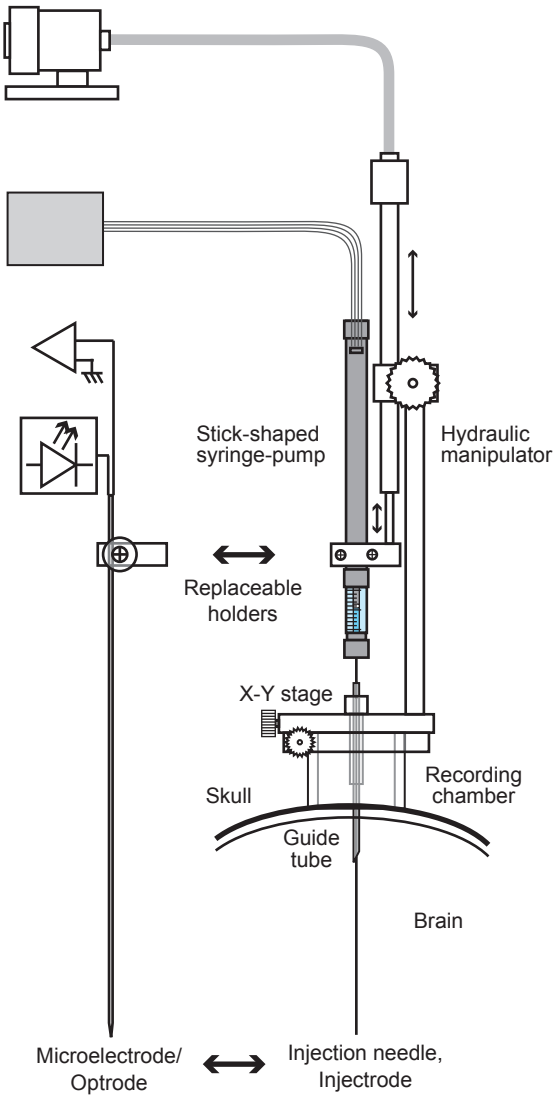
Stick-shaped
syringe-pump
Hydraulic
manipulator
Replaceable
holders
X-Y stage
Recording
chamber
Skull
Guide
tube
Brain
Microelectrode/
Optrode
Injection needle,
Injectrode

Figure 4

Figure 4. Stick-shaped ultrasmall syringe-pump system. (**A**) A photograph (top) and a schematic drawing (bottom) of the stick-shaped syringe-pump that consists of an injection needle or an injectrode (see Fig. 5), a 10-μL glass column, and a motor drive. Motor drive is controlled by a stepping motor controller on Windows PC. Please note that the unit of the scale in the top panel is in cm. (**B**) The stick-shaped syringe-pump held by a conventional micromanipulator mounted on a recording chamber attached to the head of a monkey. (**C**) A schematic drawing of the injection system for chronically-prepared monkeys. The stick-shaped syringe-pump is held by a hydraulic manipulator. Conventional microelectrode, injectrode, and the optrode can be inserted into the same horizontal coordinate through the guide tube fixed to the manipulator's x-y stage.

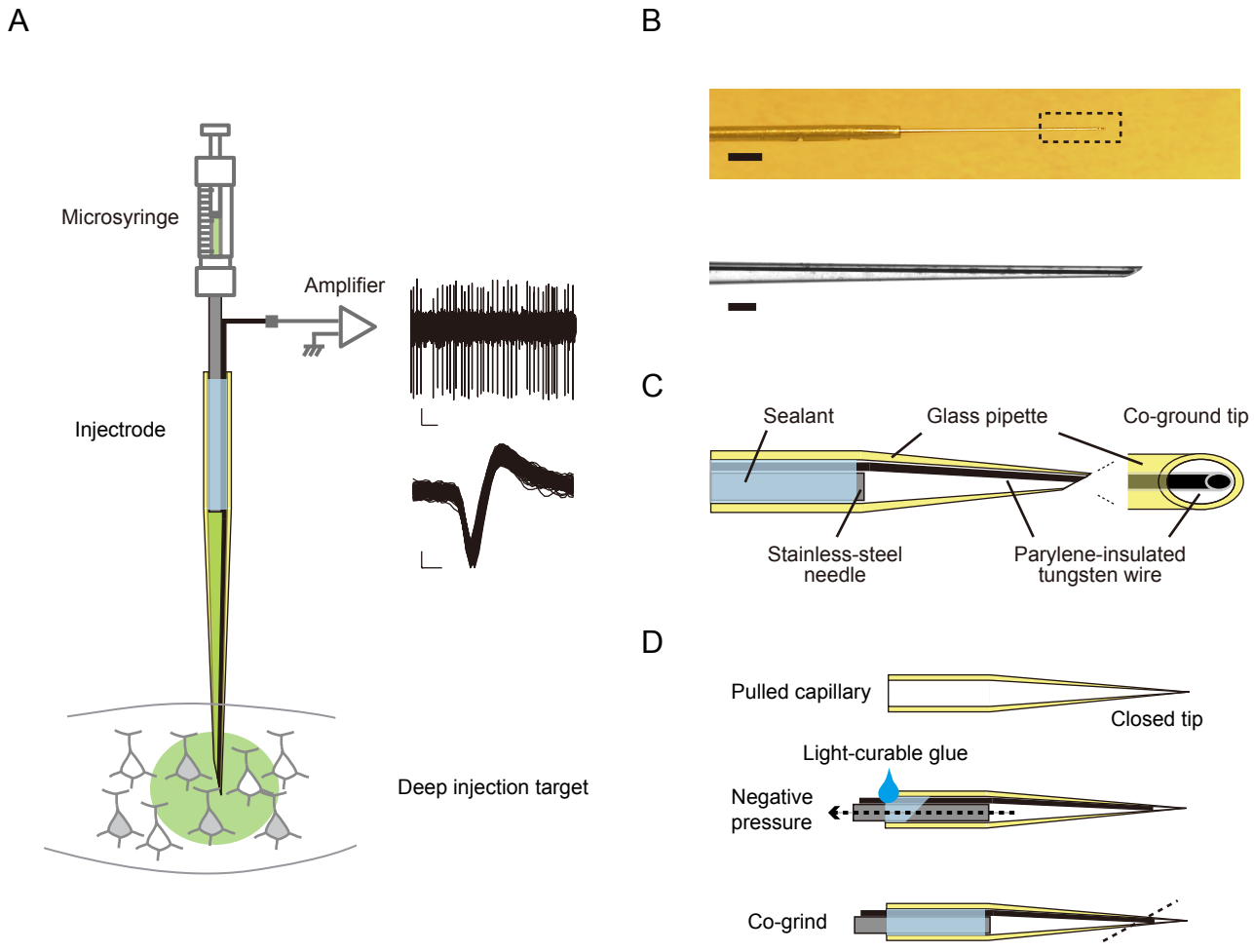
A
Microsyringe
Amplifier
Injectrode
Deep injection target
B
C
Sealant
Glass pipette
Co-ground tip
Stainless-steel needle
Parylene-insulated tungsten wire
D
Pulled capillary
Closed tip
Light-curable glue
Negative pressure
Co-grind

Figure 5

Figure 5. Metal-backboned glass injectrode. (**A**) A schematic drawing of the metal-backboned injectrode. Target region of interest can be identified by recording the neural activity at the tip of the injection needle. Inset, continuous (top) and superimposed traces of a single-unit recorded in the superior colliculus of an anesthetized rat with the injectrode enclosing a 20-μm diameter tungsten wire. Scales: top, vertical, 50 μV, horizontal, 1s; bottom, vertical 50 μV, horizontal 128 μs. (**B**) A low (top) and a high (bottom) magnification views of the metal-backboned glass injectrode. Silver part on the left end in the top panel is the stainless steel needle backbone. (**C**) A schematic drawing. A parylene-insulated tungsten wire and a stainless steel needle are enclosed within a glass pipette that is firmly sealed by adhesive. The tungsten wire is insulated by parylene and reaches to the tip of the pipette, sharing the same elliptical plane. (**D**) A schematic drawing of the fabrication procedure. First, the glass capillary with a thin closed tip is made. Second, the insulated tungsten wire and the stainless steel injection needle are inserted into the pipette. Light-curable adhesive was actively permeated by negative pressure. Third, the tips of the pipette and the wire were ground together.

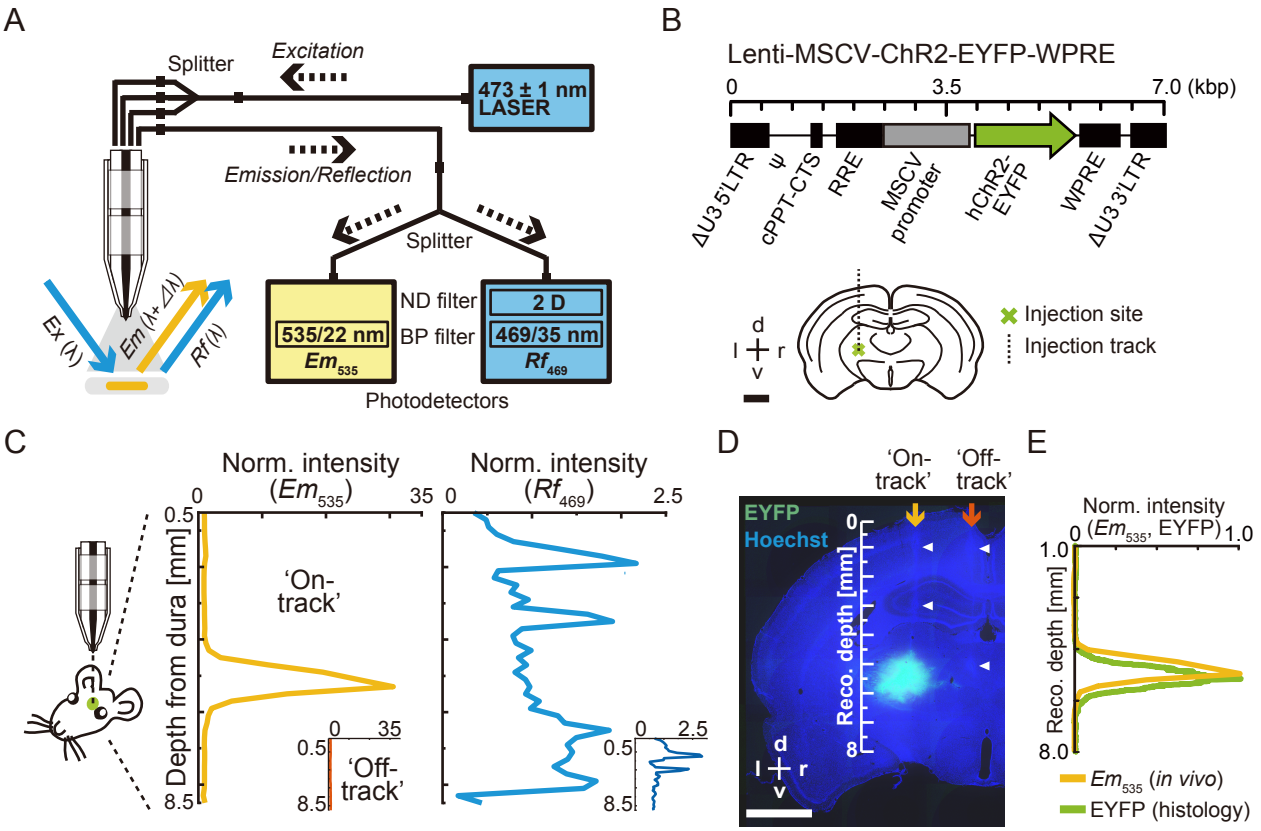
A
Splitter
Excitation
473 ± 1 nm LASER
Emission/Reflection
Splitter
Ex (λ)
Em (λ+Δλ)
Rf (λ)
535/22 nm
Em535
ND filter
BP filter
2 D
469/35 nm
Rf469
Photodetectors
B
Lenti-MSCV-ChR2-EYFP-WPRE
0
3.5
7.0 (kbp)
ΔU3 5'LTR
ψ
cPPT-CTS
RRE
MSCV promoter
hChR2-EYFP
WPRE
ΔU3 3'LTR
d
l
r
v
Injection site
Injection track
C
Norm. intensity (Em535)
Norm. intensity (Rf469)
Depth from dura [mm]
'On-track'
'Off-track'
D
'On-track'
'Off-track'
EYFP
Hoechst
Reco. depth [mm]
E
Norm. intensity (Em535, EYFP)
Reco. depth [mm]
Em535 (in vivo)
EYFP (histology)

Figure 6

Figure 6. Fiber-optic EYFP fluorescence detection *in vivo*. (**A**) A diagram of the fluorescence readout system. Three optical fibers are connected to an excitation (*Ex*) light source, while the optical path of the remaining one fiber is split and connected to either of two photodetectors installed with a bandpass (BP) filter (the 535-nm band for EYFP emission, Em_{535}, or the 469-nm band for background reflection, Rf_{469}). ND, neutral density. 2D, optical density of 2. (**B to E**) Fiber-optic fluorescence measurements and histological confirmation in the rat thalamus. (B) Top, the lentiviral vector construct; bottom, a schema for the viral injection. d, dorsal; v, ventral; r, right; l, left. Scale, 2 mm. (C) Intensity profiles of Em_{535} and Rf_{469}. “on-track”, the track penetrating the injection site; “off-track”, the track 2 mm from the “on-track”; insets, intensity profiles along the “off-track”. Profiles on these tracks were obtained with a constant excitation light power. The intensity was normalized to the baseline. (D) A coronal histological brain section corresponding to the recorded region in (C). “On-track” and “off-track” were reconstructed from the electrolytic lesion marks (white arrow heads). Vertical scale bar, reconstructed (Reco.) scale; horizontal scale bar, 2 mm on the histological section; d, dorsal; v, ventral; r, right; l, left. (E) A comparison of the Em_{535} profile obtained *in vivo* and the EYFP fluorescence profile obtained in histology. The intensity was baseline-subtracted and normalized to the maximum.

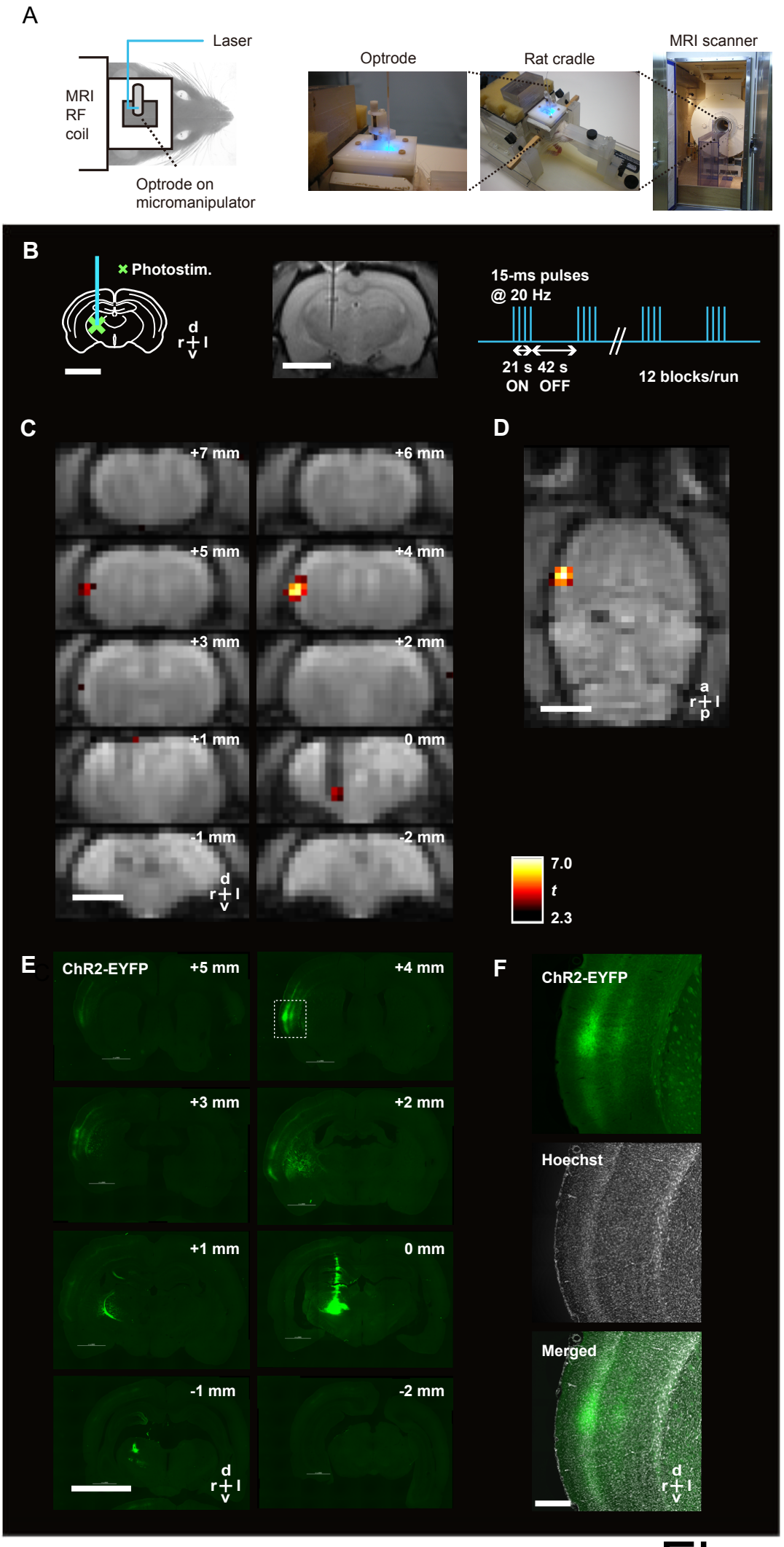
A
Laser
MRI
RF
coil
Optrode on
micromanipulator
Optrode
Rat cradle
MRI scanner
B
Photostim.
d
r l
v
15-ms pulses
@ 20 Hz
21 s 42 s
ON OFF
12 blocks/run
C
+7 mm
+6 mm
+5 mm
+4 mm
+3 mm
+2 mm
+1 mm
0 mm
-1 mm
-2 mm
D
a
r l
p
7.0
t
2.3
E
ChR2-EYFP
+5 mm
+4 mm
+3 mm
+2 mm
+1 mm
0 mm
-1 mm
-2 mm
F
ChR2-EYFP
Hoechst
Merged

Figure 7

Figure 7. fMRI during photostimulation of the rat thalamus. (**A**) Left, a schematic drawing of the experimental setup. The glass-coated optrode was held by an MRI compatible micromanipulator and mounted on the surface RF coil with a square window (the left image). The RF coil was mounted on the rat cradle (the middle image) to set in the MRI scanner (the right image). (**B**) Left, a schematic drawing of the photostimulation site, the thalamic posterior medial nucleus (POm). Middle, a high-resolution anatomical image in coronal orientation showing the optrode track. Right, the photostimulation protocol. Scale bars, 5 mm. Note that the optrode thickness is enhanced due to the susceptibility artifact [23]. (**C**) A series of activation maps ($t>2.33$, $P<0.01$, uncorrected) from a contrast stimulation-ON versus stimulation-OFF that are overlaid on EPI images in 1 mm interval. “0-mm” slice corresponds to the stimulation site identified by the optrode. Scale bar, 5 mm. (**D**) A horizontal image at the cortical activation site. Scale bar, 5 mm. (**E**) A series of histological sections in 1 mm interval. “0-mm” slice corresponds to the virus injection and photostimulation site identified by the track. Scale bar, 5 mm. (**F**) Magnified views of an adjacent section of the “4-mm” slice in (E), stained for nuclei by Hoechst. Scale bar, 300 μm.

A

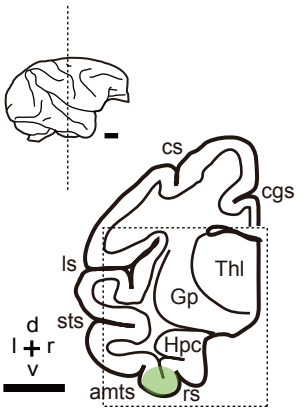
cs
cgs
ls
Thl
Gp
sts
Hpc
amts
rs
d
l + r
v

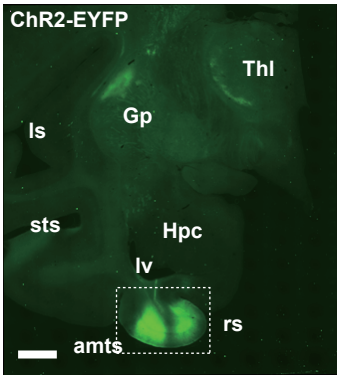
ChR2-EYFP
Thl
Gp
ls
sts
Hpc
lv
rs
amts

B

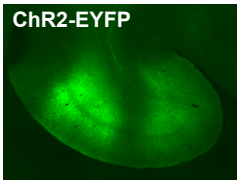
ChR2-EYFP

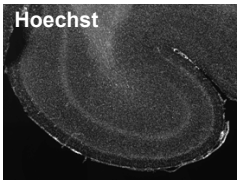
Hoechst

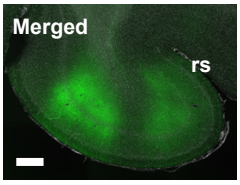
Merged
rs

C

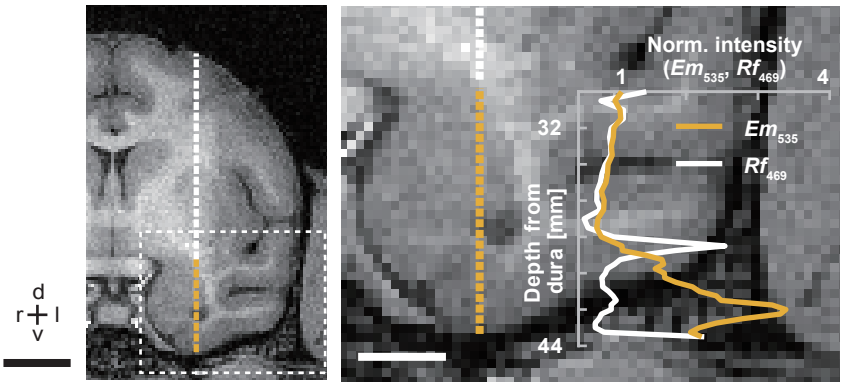
d
r + l
v
Norm. intensity
(Em535, Rf469)
1
4
32
44
Em535
Rf469
Depth from
dura [mm]

Figure 8

Figure 8. Gene transfer into the macaque perirhinal cortex. (**A**) Injection of an adeno-accociated virus vector, AAV5-CaMKIIa-ChR2(H134R)-EYFP into the perirhinal cortex of the macaque monkeys. Left, schematic drawings of lateral (top) and coronal (bottom) views of the macaque brain. Scale bars, 10 mm. Right, a fluorescent image of a monkey brain, corresponding to the dotted rectangular region in the left drawing. Scale bar, 3 mm. Gp, globus pallidus; Hpc, hippocampus; Thl, thalamus; amts, anterior medial temporal sulcus; cgs, cingulate sulcus; ls, lateral sulcus; lv, lateral ventricle; rs, rhinal sulcus; sts, superior temporal sulcus. (**B**) Magnified views of the perirhinal cortex on an adjacent section of the section in (A), stained by Hoechst to visualize cortical layers. Scale bar, 1 mm. Note two separate injection tracks. (**C**) Fiber-optically measured fluorescence profile in the brain of another monkey. Left, a para-coronal MRI image showing a putative optrode track position. Yellow region indicate the depth range of fluorescence measurements. Scale bar, 10 mm. Right, the intensity profiles of Em_{535} and Rf_{469} overlaid on the magnified MRI image so that the depths of the MRI image and the fluorescence profile correspond to each other. The light intensity was normalized to the baseline. Scale bar, 5 mm.

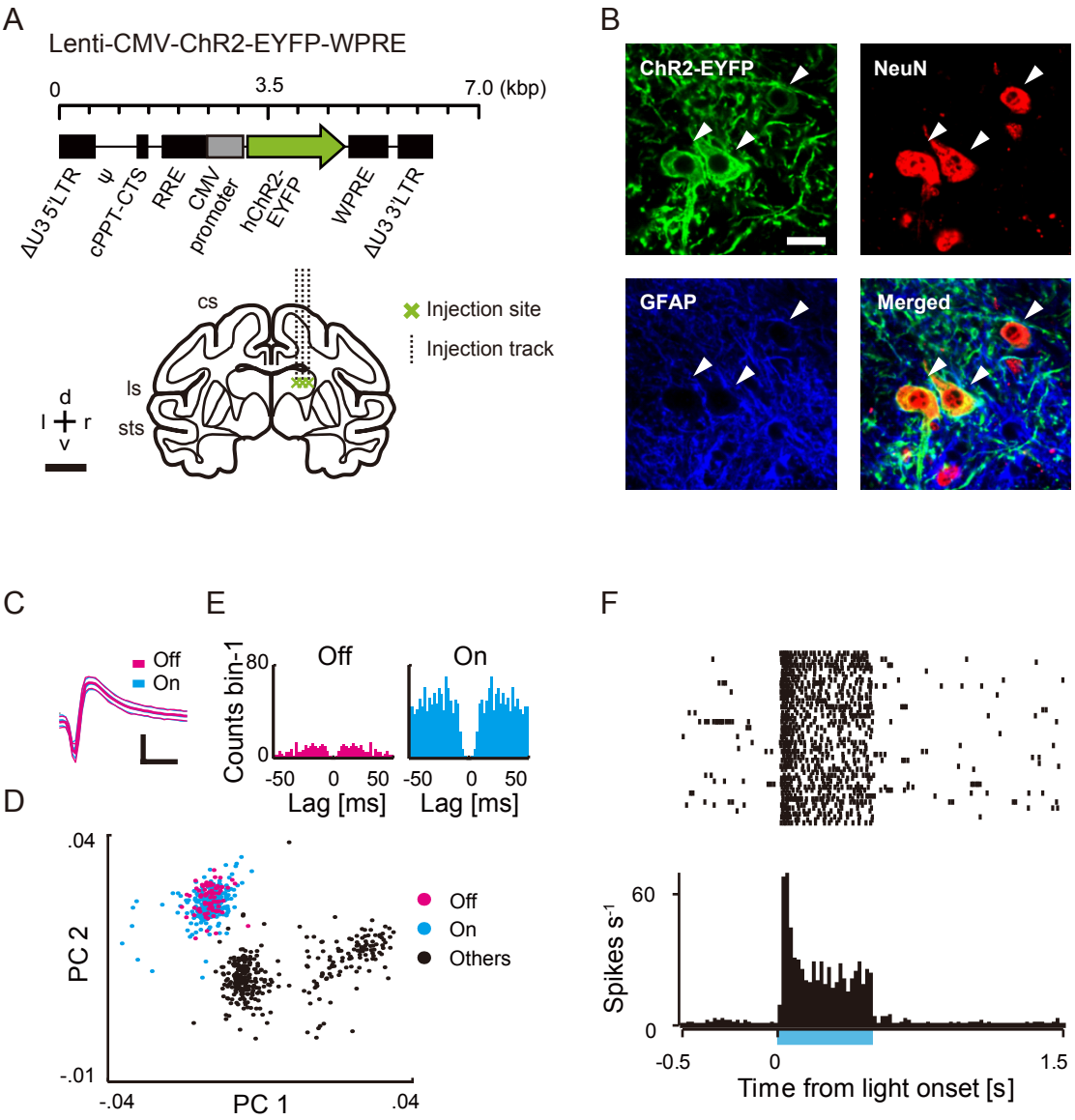
A
Lenti-CMV-ChR2-EYFP-WPRE
0
3.5
7.0 (kbp)
ΔU3 5'LTR
ψ
cPPT-CTS
RRE
CMV promoter
hChR2-EYFP
WPRE
ΔU3 3'LTR
cs
ls
sts
d
l
r
v
Injection site
Injection track
B
ChR2-EYFP
NeuN
GFAP
Merged
C
Off
On
D
.04
-.01
-.04
PC 2
PC 1
.04
Off
On
Others
E
Off
On
Counts bin-1
80
0
-50
0
50
Lag [ms]
F
60
0
Spikes s-1
-0.5
0
1.5
Time from light onset [s]

Figure 9

Figure 9. Photostimulation and recording of single-unit activity in the macaque thalamus. (**A**) Top, the lentiviral vector construct; bottom, a schema for the viral injections. cs, central sulcus; ls, lateral sulcus; sts, superior temporal sulcus; d, dorsal; v, ventral; r, right; l, left; scale bar, 10 mm. (**B**) Immunohistochemical images for ChR2-EYFP, a neuronal marker NeuN and a glial marker GFAP. Arrow heads, ChR2-EYFP-expressing neurons. Scale bar, 25 μm. (**C to F**) Single-unit separation during photostimulation. (C) Spike waveforms (mean +/- SD) of an exemplar unit during light-off (red) and light-on (blue) periods. Scales: vertical, 25 μV; horizontal, 1000 μs. (D) Scatter plot of principal components (PC1 and PC2) of the spike waveforms. Only one third of the total spikes are plotted for display purpose. Magenta, the same unit during light-off period; cyan, the same unit during light-on period; black, other units. (E) Autocorrelograms of the same unit during light-off (magenta) and light-on (cyan) periods. Note that the total number of spikes is larger in light-on period than in light-off period. (F) Response to the photostimulation. Top, raster plot; bottom, PSTH. Blue horizontal bar, photostimulation period.

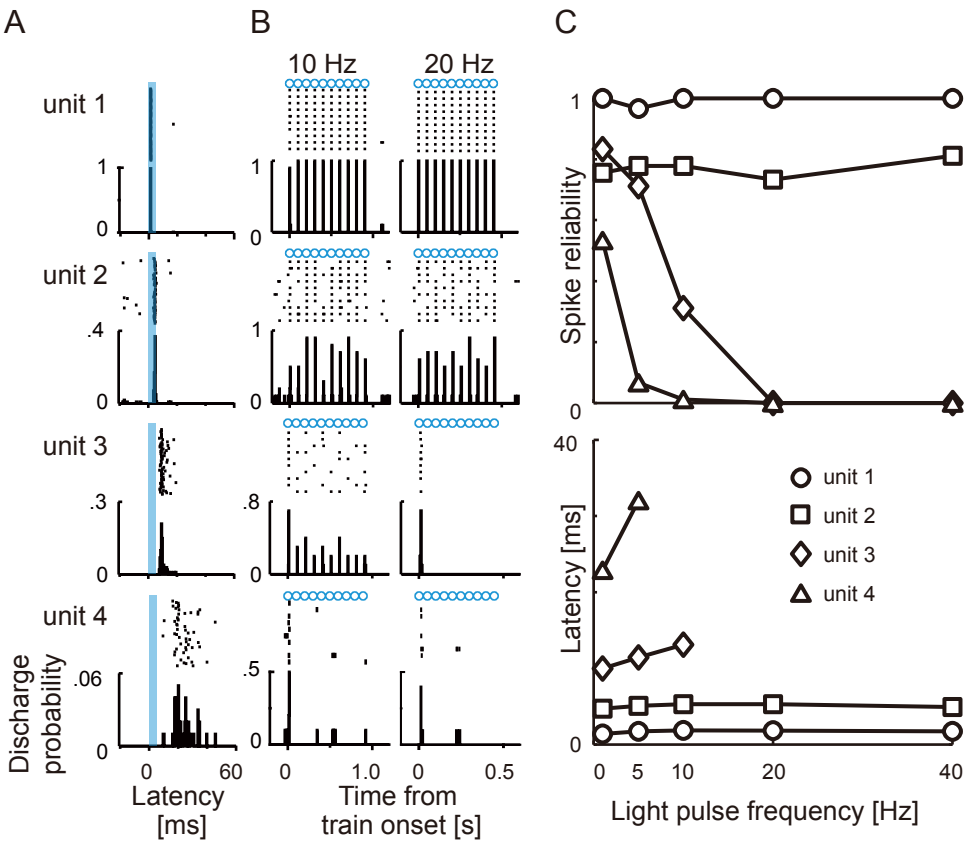
A
B
C
10 Hz
20 Hz
unit 1
unit 2
unit 3
unit 4
Discharge probability
Latency [ms]
Time from train onset [s]
Spike reliability
Latency [ms]
Light pulse frequency [Hz]
unit 1
unit 2
unit 3
unit 4

Figure 10

Figure 10. Single-unit responses to the repetitive short light pulses. (**A**) Action potential generation at 1 Hz. Top of each unit, raster plot; bottom of each unit, histogram of spike latency. Blue shaded periods, photostimulation periods (5-ms duration). (**B**) Spike response reliabilities at 10 and 20 Hz. Top of each unit, raster plot; bottom of each unit, PSTH triggered by the onset of pulse train. Blue circle, timing of light pulses (5 ms). (**C**) Spike response reliability (top) and spike latency (bottom) as a function of light pulse frequency.

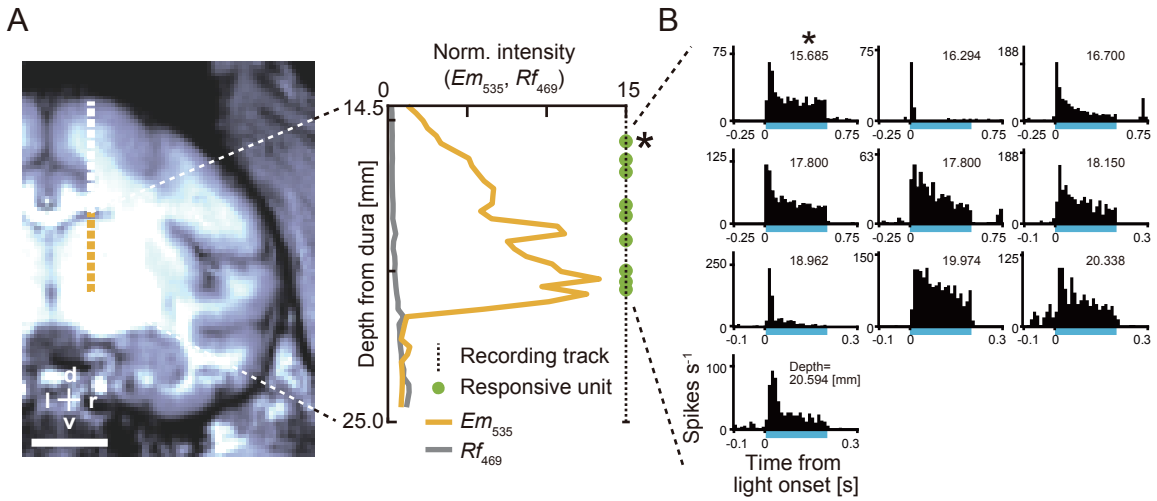
A
B
d
l
r
v
Norm. intensity
(Em_{535}, Rf_{469})
0
15
14.5
25.0
Depth from dura [mm]
Recording track
Responsive unit
Em_{535}
Rf_{469}
*
15.685
16.294
16.700
17.800
17.800
18.150
18.962
19.974
20.338
Depth=
20.594 [mm]
Spikes s^{-1}
Time from
light onset [s]

Figure 11

Figure 11. Distributions of light-responsive units and EYFP fluorescence. (**A**) Left, the putative position of a recording track near viral injection sites schematically illustrated on the corresponding MRI image (vertical dotted line). The yellow region represents the putative recorded region (from 15 mm to 25 mm from dura). Right, the profiles of Em_{535}, Rf_{469} and light-responsive single units along the same track. Light intensities were normalized to the baseline. Scale bar, 10 mm. (**B**) PSTHs for all light-responsive single-units encountered along the track in (A). The unit with an asterisk corresponds to the unit with the asterisk in (A).

ACKNOWLEDGEMENTS

I would like to express my greatest appreciation to Professor Yasushi Miyashita for his enthusiasm for my education. I would especially like to thank Dr. Yohei Ohashi for the production of lentiviral vectors, and would also like to thank Dr. Tadashi Tsubota, Dr. Yusuke Adachi, Dr. Daigo Takeuchi, Dr. Toshiyuki Hirabayashi, Dr. Masae Yaguchi, Dr. Makoto Matsuyama, and Mr. Takeru Sekine for collaboration; Dr. Teppei Matsui, Dr. Kenji W. Koyano, Dr. Takahiro Osada, Dr. Kentaro Miyamoto, Dr. Rieko Setsuie for their kind help and beneficial discussions; and Ms. Ayumi Fukuda and Ms. Tomomi Watanabe for their indispensable assistance.

I would like to express my gratitude to my family for their continuous support of my passion for science. My deepest appreciation goes to my wife, Dr. Mayuko Tamura, for standing by me in all situations.

A part of works described in this thesis has been published [12] on the Journal of Neuroscience Methods from Elsevier.

REFERENCES

[1] Liu X, Ramirez S, Pang PT, Puryear CB, Govindarajan A, Deisseroth K, Tonegawa S. Optogenetic stimulation of a hippocampal engram activates fear memory recall. ***Nature***, 484: 381-5 (2012).

[2] Goshen I, Brodsky M, Prakash R, Wallace J, Gradinaru V, Ramakrishnan C, Deisseroth K. Dynamics of Retrieval Strategies for Remote Memories. ***Cell***, 147: 678-89 (2011).

[3] Xu W, Südhof TC. A Neural Circuit for Memory Specificity and Generalization. ***Science***, 339: 1290-5 (2013).

[4] Miyashita Y. Cognitive memory: cellular and network machineries and their top-down control. ***Science***, 306: 435-40 (2004).

[5] Naya Y, Yoshida M, Miyashita Y. Forward processing of long-term associative memory in monkey inferotemporal cortex. ***J Neurosci***, 23: 2861-71 (2003).

[6] Miyashita Y. Neuronal correlate of visual associative long-term memory in the primate temporal cortex. ***Nature***, 335: 817-20 (1988).

[7] Mattis J, Tye KM, Ferenczi EA, Ramakrishnan C, O'Shea DJ, Prakash R, Gunaydin LA, Hyun M, Fenno LE, Gradinaru V, Yizhar O, Deisseroth K. Principles for applying optogenetic tools derived from direct comparative analysis of microbial opsins. ***Nat Methods***, 9: 159-72 (2012).

[8] Cavanaugh J, Monosov I, McAlonan K, Berman R, Smith M, Cao V, Wang K, Boyden E, Wurtz R. Optogenetic Inactivation Modifies Monkey Visuomotor Behavior. ***Neuron***, 76: 901-7 (2012).

[9] Jazayeri M, Lindbloom-Brown Z, Horwitz GD. Saccadic eye movements evoked by optogenetic activation of primate V1. ***Nat Neurosci***, 15: 1368-70 (2012).

[10] Gradinaru V, Thompson KR, Zhang F, Mogri M, Kay K, Schneider MB, Deisseroth K. Targeting and readout strategies for fast optical neural control in vitro and in vivo. ***J Neurosci***, 27: 14231-8 (2007).

[11] Diester I, Kaufman MT, Mogri M, Pashaie R, Goo W, Yizhar O, Ramakrishnan C, Deisseroth K, Shenoy KV. An optogenetic toolbox designed for primates. ***Nat Neurosci***, 14: 387-97 (2011).

[12] Tamura K, Ohashi Y, Tsubota T, Takeuchi D, Hirabayashi T, Yaguchi M, Matsuyama M, Sekine T, Miyashita Y. A glass-coated tungsten microelectrode enclosing optical fibers for optogenetic exploration in primate deep brain structures. ***J Neurosci Methods***, 211: 49-57 (2012).

[13] Lee JH, Durand R, Gradinaru V, Zhang F, Goshen I, Kim DS, Fenno LE, Ramakrishnan C, Deisseroth K. Global and local fMRI signals driven by neurons defined optogenetically by type and wiring. ***Nature***, 465: 788-92 (2010).

[14] Lima SQ, Hromadka T, Znamenskiy P, Zador AM. PINP: a new method of tagging neuronal populations for identification during in vivo electrophysiological recording. ***PLoS ONE***, 4: e6099 (2009).

[15] ***The Rat Brain in STEREOTAXIC COORDINATES***, Paxinos G, Watson C (1998).

[16] ***A Combined MRI and Histology Atlas of the Rhesus Monkey Brain in Stereotaxic Coordinates, First Edition***, Saleem KS, Logothetis NK (2007).

[17] Nikkhah G, Olsson M, Eberhard J, Bentlage C, Cunningham MG, Bjorklund A. A microtransplantation approach for cell suspension grafting in the rat Parkinson model: a detailed account of the methodology. ***Neuroscience***, 63: 57-72 (1994).

[18] Ohashi Y, Tsubota T, Sato A, Koyano KW, Tamura K, Miyashita Y. A bicistronic lentiviral vector-based method for differential transsynaptic tracing of neural circuits. ***Mol Cell Neurosci***, 46: 136-47 (2011).

[19] Tsubota T, Ohashi Y, Tamura K, Sato A, Miyashita Y. Optogenetic manipulation of cerebellar purkinje cell activity in vivo. ***PLoS One***, 6: e22400 (2011).

[20] Hanawa H, Hematti P, Keyvanfar K, Metzger ME, Krouse A, Donahue RE, Kepes S, Gray J, Dunbar CE, Persons DA, Nienhuis AW. Efficient gene transfer into rhesus repopulating hematopoietic stem cells using a simian immunodeficiency virus-based lentiviral vector system. ***Blood***, 103: 4062-9 (2004).

[21] Miyoshi H, Blomer U, Takahashi M, Gage FH, Verma IM. Development of a self-inactivating lentivirus vector. ***J Virol***, 72: 8150-7 (1998).

[22] Matsui T, Tamura K, Koyano KW, Takeuchi D, Adachi Y, Osada T, Miyashita Y. Direct comparison of spontaneous functional connectivity and effective connectivity measured by intracortical microstimulation: an fMRI study in macaque monkeys. ***Cereb Cortex***, 21: 2348-56 (2011).

[23] Matsui T, Koyano KW, Koyama M, Nakahara K, Takeda M, Ohashi Y, Naya Y, Miyashita Y. MRI-based localization of electrophysiological recording sites within the cerebral cortex at single-voxel accuracy. ***Nat Methods***, 4: 161-8 (2007).

[24] Bradley PMJ, Murphy D, Kasparov S, Croker J, Paton JFR. A micro-optrode for simultaneous extracellular electrical and intracellular optical recording from neurons in an intact oscillatory neuronal network. ***J Neurosci Methods***, 168: 383-95 (2008).

[25] Matsui T, Koyano KW, Tamura K, Osada T, Adachi Y, Miyamoto K, Chikazoe J, Kamigaki T, Miyashita Y. FMRI activity in the macaque cerebellum evoked by intracortical microstimulation of the primary somatosensory cortex: evidence for polysynaptic propagation. ***PLoS One***, 7: e47515 (2012).

[26] Genovese CR, Lazar NA, Nichols T. Thresholding of statistical maps in functional neuroimaging using the false discovery rate. ***Neuroimage***, 15: 870-8 (2002).

[27] Kravitz AV, Freeze BS, Parker PRL, Kay K, Thwin MT, Deisseroth K, Kreitzer AC. Regulation of parkinsonian motor behaviours by optogenetic control of basal ganglia circuitry. ***Nature***, 466: 622-6 (2010).

[28] Takeuchi D, Hirabayashi T, Tamura K, Miyashita Y. Reversal of interlaminar signal between sensory and memory processing in monkey temporal cortex. ***Science***, 331: 1443-7 (2011).

[29] Lechasseur Y, Dufour S, Lavertu G, Bories C, Deschenes M, Vallee R, De Koninck Y. A microprobe for parallel optical and electrical recordings from single neurons in vivo. ***Nat Methods***, 8: 319-25 (2011).

[30] Hirabayashi T, Takeuchi D, Tamura K, Miyashita Y. Triphasic dynamics of stimulus-dependent information flow between single neurons in macaque inferior temporal cortex. ***J Neurosci***, 30: 10407-21 (2010).

[31] Cohen JY, Haesler S, Vong L, Lowell BB, Uchida N. Neuron-type-specific signals for reward and punishment in the ventral tegmental area. ***Nature***, 482: 85-8 (2012).

[32] Kravitz AV, Kreitzer AC. Optogenetic manipulation of neural circuitry in vivo. ***Curr Opin Neurobiol***, 21: 433-9 (2011).

[33] Royer S, Zemelman BV, Barbic M, Losonczy A, Buzsaki G, Magee JC. Multi-array silicon probes with integrated optical fibers: light-assisted perturbation and recording of local neural circuits in the behaving animal. ***Eur J Neurosci***, 31: 2279-91 (2010).

[34] Zhang J, Laiwalla F, Kim JA, Urabe H, Van Wagenen R, Song YK, Connors BW, Zhang F, Deisseroth K, Nurmikko AV. Integrated device for optical stimulation and spatiotemporal electrical recording of neural activity in light-sensitized brain tissue. ***J Neural Eng***, 6: 055007 (2009).

[35] Quintana J, Fuster JM. A microelectrode for depth recording in awake animals.

Electroencephalogr Clin Neurophysiol, 63: 83-5 (1986).

[36] Levick WR. Another tungsten microelectrode. ***Med Biol Eng Comput***, 10: 510-5 (1972).

[37] Merrill E, Ainsworth A. Glass-coated platinum-plated tungsten microelectrodes. ***Med Biol Eng Comput***, 10: 662-72 (1972).

[38] Sugiyama K, Dong WK, Chudler EH. A simplified method for manufacturing glass-insulated metal microelectrodes. ***J Neurosci Methods***, 53: 73-80 (1994).

[39] Zhang F, Gradinaru V, Adamantidis AR, Durand R, Airan RD, de Lecea L, Deisseroth K. Optogenetic interrogation of neural circuits: technology for probing mammalian brain structures. ***Nat Protoc***, 5: 439-56 (2010).

[40] Cardin JA, Carlen M, Meletis K, Knoblich U, Zhang F, Deisseroth K, Tsai LH, Moore CI. Targeted optogenetic stimulation and recording of neurons in vivo using cell-type-specific expression of Channelrhodopsin-2. ***Nat Protoc***, 5: 247-54 (2010).

[41] ***Lentivirus Gene Engineering Protocols***, Federico M, 299-307 (2003).

[42] Kliem MA, Wichmann T. A method to record changes in local neuronal discharge in response to infusion of small drug quantities in awake monkeys. ***J Neurosci Methods***, 138: 45-9 (2004).

[43] Martin JH, Ghez C. Pharmacological inactivation in the analysis of the central control of movement. ***J Neurosci Methods***, 86: 145-59 (1999).

[44] Dias EC, Segraves MA. A pressure system for the microinjection of substances into the brain of awake monkeys. ***J Neurosci Methods***, 72: 43-7 (1997).

[45] Perrett DI, Rolls ET. A technique for microiontophoretic study of single neurones in the behaving monkey. ***J Neurosci Methods***, 12: 289-95 (1985).

[46] Inagaki K, Heiney SA, Blazquez PM. Method for the construction and use of carbon fiber multibarrel electrodes for deep brain recordings in the alert animal. ***J Neurosci Methods***, 178: 255-62 (2009).

[47] Li BM, Mei ZT, Kubota K. Multibarreled glass-coated tungsten microelectrode for both neuronal activity recording and iontophoresis in monkeys. ***Neurosci Res***, 8: 214-9 (1990).

[48] Haidarliu S, Shulz D, Ahissar E. A multi-electrode array for combined microiontophoresis and multiple single-unit recordings. ***J Neurosci Methods***, 56: 125-31 (1995).

[49] Hellier M, Boers P, Lambert GA. Fabrication of a metal-cored multi-barrelled microiontophoresis assembly. ***J Neurosci Methods***, 32: 55-61 (1990).

[50] Malpeli JG. Reversible inactivation of subcortical sites by drug injection. ***J Neurosci Methods***, 86: 119-28 (1999).

[51] Christie IN, Wells JA, Southern P, Marina N, Kasparov S, Gourine AV, Lythgoe MF. fMRI response to blue light delivery in the naive brain: Implications for combined optogenetic fMRI studies. ***Neuroimage***, 66C: 634-41 (2012).

[52] Woeffler-Maucler C, Beghin A, Ressnikoff D, Bezin L, Marinesco S. Automated immunohistochemical method to quantify neuronal density in brain sections: application to neuronal loss after status epilepticus. ***J Neurosci Methods***, 225: 32-41 (2014).

[53] ***The Synapcic Organization of The Brain 5th edition***, Shepherd GM, 311-59 (2004).

[54] Kim MJ, Kim YB, Kang KJ, Huh N, Oh JH, Kim Y, Jung MW. Neuronal interactions are higher in the cortex than thalamus in the somatosensory pathway. ***Neuroscience***, 118: 205-16 (2003).

[55] Viaene AN, Petrof I, Sherman SM. Properties of the thalamic projection from the posterior medial nucleus to primary and secondary somatosensory cortices in the mouse. ***Proc Natl Acad Sci U S A***, 108: 18156-61 (2011).

[56] ***Neuronal Network Analysis***, Fellin T, Halassa M, 339-55 (2012).

[57] Schulz K, Sydekum E, Krueppel R, Engelbrecht CJ, Schlegel F, Schroter A, Rudin M, Helmchen F. Simultaneous BOLD fMRI and fiber-optic calcium recording in rat neocortex. ***Nat Methods***, 9: 597-602 (2012).

[58] Cui G, Jun SB, Jin X, Pham MD, Vogel SS, Lovinger DM, Costa RM. Concurrent activation of striatal direct and indirect pathways during action initiation. ***Nature***, 494: 238-42 (2013).

[59] Naya Y, Yoshida M, Miyashita Y. Backward spreading of memory-retrieval signal in the primate temporal cortex. ***Science***, 291: 661-4 (2001).

[60] Sherman SM. Tonic and burst firing: dual modes of thalamocortical relay. ***Trends Neurosci***, 24: 122-6 (2001).

[61] Gerits A, Vanduffel W. Optogenetics in primates: a shining future? ***Trends Genet***, 29: 403-11 (2013).

[62] Kushibiki T, Okawa S, Hirasawa T, Ishihara M. Optogenetics: Novel Tools for Controlling Mammalian Cell Functions with Light. ***Int J Photoen***, 2014: Article ID 895039 (2014).

[63] Mandal R, Nag S, Thakor NV. Wirelessly powered and controlled, implantable, multi-channel, multi-wavelength optogenetic stimulator. ***2013 IEEE MTT-S International Microwave Workshop Series on RF and Wireless Technologies for Biomedical and Healthcar***: DOI: 10.1109/IMWS-BIO.2013.6756181 (2013).